Kinematic dynamos and resolution limits for Smoothed Particle Magnetohydrodynamics

Nikyta Shchutskyi,[1,2]★ Matthieu Schaller,[1,2] Orestis A. Karapiperis,[1,2] Federico A. Stasyszyn[3,4] & Axel Brandenburg[5,6]

[1]Lorentz Institute for Theoretical Physics, Leiden University, PO Box 9506, NL-2300 RA Leiden, The Netherlands
[2]Leiden Observatory, Leiden University, PO Box 9513, NL-2300 RA Leiden, The Netherlands
[3]Instituto de Astronomíca Teórica y Experimental (IATE), CONICET – UNC, Laprida 854, X5000BGR Córdoba, Argentina
[4]Observatorio Astronómico, Universidad Nacional de Córdoba, Laprida 854, X5000BGR Córdoba, Argentina
[5]Nordita, KTH Royal Institute of Technology and Stockholm University, Hannes Alfvéns väg 12, SE-10691 Stockholm, Sweden
[6]The Oskar Klein Centre, Department of Astronomy, Stockholm University, AlbaNova, SE-10691 Stockholm, Sweden

Accepted XXX. Received YYY; in original form ZZZ

ABSTRACT

Understanding the origin and evolution of magnetic fields on cosmological scales opens up a window into the physics of the early Universe. Numerical simulations of such fields require a careful treatment to faithfully solve the equations of magnetohydrodynamics (MHD) without introducing numerical artefacts. In this paper, we study the growth of the magnetic fields in controlled kinematic dynamo setups using both smoothed particle hydrodynamics implementations in the Swift code. We assess the quality of the reconstructed solution in the Roberts flow case against the reference implementation in the Pencil code and find generally a good agreement. Similarly, we reproduce the known features of the more complex ABC flow. Using a simple induction-diffusion balance model to analyse the results, we construct an "overwinding" trigger metric to locally detect regions where the magnetic diffusion cannot counteract the expected induction because of limitations in the method's ability to resolve magnetic field gradients. This metric is then used to identify the necessary resolution and resistivity levels to counteract the overwinding problem. We finally apply this metric to adiabatic cosmological simulations and discuss the resolution requirements needed to resolve the growth of the primordial fields without artefacts.

Key words: magnetohydrodynamics – dynamo – methods: numerical – cosmology: theory

1 INTRODUCTION

Astrophysical observations, such as rotation measure and synchrotron emission, indicate the presence of magnetic fields on the scale of galaxies and the intergalactic medium. Similarly, the absence of secondary X-ray signals from blazars sets a lower bound on the magnetic field strength in cosmic voids (Neronov & Vovk 2010). Magnetic fields are thus expected to be found embedded all the way to the large-scale structure of the Universe. For comprehensive reviews, see Han (2017) and Korochkin et al. (2021). Despite the ubiquitous evidence of their presence, the origin of the magnetic fields on cosmic scales is still unknown. For instance, magnetic fields may have originated in the early Universe, emerging during inflation, electroweak, or QCD phase transitions; see Durrer & Neronov (2013) for a review of these mechanisms. The study of such fields would thus open a window towards understanding fundamental physics processes in the early Universe, possibly much before nucleosynthesis. Alternatively, these magnetic fields could have formed in astrophysical objects through battery mechanisms (e.g. Biermann & Schlüter 1951; Langer & Durrive 2018; Attia et al. 2021; Mikhailov & Andreasyan 2021).

Irrespective of their origin, magnetic fields grow through gravitational collapse and undergo exponential amplification via dynamo processes in dense astrophysical environments such as galaxies (e.g. Brandenburg & Ntormousi 2023). This amplification erases any memory of initial conditions and ceases once the fields become dynamically significant, influencing gas motion, i.e. saturating close to an energy equipartition regime (e.g. Ruzmaikin et al. 1988; Rogachevskii 2021). Studying magnetic fields as a window onto the early Universe thus requires us to focus on regions of space where these dynamo mechanisms are not dominant.

As such, the intergalactic medium (IGM) could serve as a reservoir for unaltered primordial magnetic fields. However, numerical studies suggest that voids and the IGM may be contaminated by magnetic fields expelled from dense astrophysical objects, for instance through AGN activity in clusters. This pollution could even reach a significant volume-filling fraction of the IGM (e.g. Arámburo-García et al. 2021), potentially influencing rotation measure (RM) and X-ray observations of magnetic fields in these regions (e.g. Arámburo-García et al. 2022; Bondarenko et al. 2022). The recent work of Tjemsland et al. (2024) shows that the fraction of space filled by a strong inter-

★ E-mail: shchutskyi@lorentz.leidenuniv.nl

galactic magnetic fields has to be at least 67%. This likely excludes most astrophysical production scenarios.

In order to make theoretical predictions, the large-scale evolution of magnetic fields can be investigated using cosmological simulations. These simulations typically employ the magnetohydrodynamics (MHD) approximation, which neglects relativistic effects, plasma effects, and treats the gas as a compressible conducting fluid in equilibrium. The equation of state is assumed to be an ideal gas with an adiabatic index $\gamma = 5/3$.

Simulations provide insight into the large-scale distribution of magnetic fields. Combined with sub-grid models for galaxy formation, such simulations are a powerful tool to predict the non-linear evolution of matter and the coupling with magnetic fields; see for instance Vogelsberger et al. (2020) for an overview of cosmological simulation methods.

Quantitatively studying magnetic fields in void environments and in the IGM requires simulations that cover large scales for statistical accuracy while maintaining sufficient resolution to capture processes relevant to magnetic field evolution. In the largest cosmological simulations with box sizes of $L_{\rm box} \sim 100\,{\rm Mpc}$ to $> 1\,{\rm Gpc}$, the mass resolution typically ranges from $m_{\rm gas} \simeq 10^6$ to $10^9\ {\rm M}_\odot$ (e.g. Dolag & Stasyszyn 2009; Nelson et al. 2019; Schaye et al. 2023) or, equivalently, the spatial resolution is only 1–10 kpc in the most dense regions (e.g. Vazza et al. 2014; Kaviraj et al. 2017). Given that the gas mass of a Milky Way-sized galaxy is around $10^{11}{\rm M}_\odot$, each such galaxy is resolved by 10^2 to 10^5 gas particles. For comparison, MHD studies of the magnetic field evolution in isolated galaxies typically employ $\gtrsim 10^5$ resolution elements (e.g. Wang & Abel 2009; Pakmor & Springel 2013; Rieder & Teyssier 2016; Pfrommer et al. 2022). Some of the magnetic field amplification processes are thus possibly under-resolved in large-scale simulations, which can be compensated by sub-grid processes akin to large-eddy-simulation approximations (Vazza et al. 2020; Liu et al. 2022).

In addition to resolution, cosmological MHD simulations also deal with large magnetic Reynolds numbers, $R_{\rm m}$

$$R_{\rm m} = \frac{v_{\rm rms}}{\eta k_0}, \tag{1}$$

where $v_{\rm rms}$ is the root mean square velocity over the simulation volume, $k_0 = 2\pi/\lambda$ is the characteristic wavenumber at length scale λ, and η is the plasma resistivity. MHD simulations of galaxy clusters suggest a good match with the observed shape of the magnetic field for turbulent resistivity values of $\eta \approx 6 \cdot 10^{27}{\rm cm}^2\ {\rm s}^{-1}$ (Bonafede et al. 2011). Assuming a typical Virial radius of $R_{\rm vir} \simeq 2.5{\rm Mpc}$ and a cluster velocity of $v_{\rm vir} \sim 10^3{\rm km\ s}^{-1}$, these values lead to magnetic Reynolds numbers $R_{\rm m} \simeq 10^3$ to 10^4.

However, semi-analytical dynamo studies in the cosmological context provide a wider range of estimates for magnetic Reynolds numbers. These studies, which consider various turbulence models and gas densities, suggest that magnetic Reynolds numbers can range from $R_{\rm m} \geq 100$ to 2000 (Schekochihin et al. 2005) or up to $R_{\rm m} \sim 10^{17}$ (Schober et al. 2012). The resolution requirements to directly simulate on cosmological scales with such Reynolds numbers is much beyond current and future computing capabilities, and here again, sub-grid process are often employed to model the unresolved part of the turbulence cascade. Alternatively, some simulations consider neglecting sub-grid effects and restrict their analysis to the well-resolved regime (Marinacci et al. 2015; Mtchedlidze et al. 2022).

The MHD differential equations can be solved numerically using various methods. Most simulations employ mesh-based approaches, such as Arepo, (Pakmor et al. 2011) and Enzo (Bryan et al. 2014). Alternatively, meshless schemes like meshless finite mass (MFM) in Gizmo (Hopkins & Raives 2015), SPH-based MHD approaches such as the ones in the Gadget code (Dolag & Stasyszyn 2009; Stasyszyn et al. 2012), Gasoline (Wissing & Shen 2020) or SPH MHD implementation in Gizmo (Hopkins & Raives 2015) have also been used for astrophysical and cosmological simulations.

In this study, we make use of Swift, an open-source SPH-based code for large-scale cosmological simulations (Schaller et al. 2024), offering several models for hydrodynamics and sub-grid physics. The code also includes two variants for SPMHD: one based one the direct integration of $\mathbf{B}/\rho$ (Karapiperis et al. 2025), inspired by the implementation of Price et al. (2018), and the other using a vector potential approach, $\mathbf{B} = \mathrm{curl}\,\mathbf{A}$, derived from the work of Stasyszyn & Elstner (2015). Having several independent numerical results with different hydrodynamics models, sub-grid models, and two MHD implementations can be advantageous for estimating the numerical uncertainty of the results.

In this work, both MHD flavors provided in Swift will be tested on a set of standard kinematic large-scale dynamo problems: the Roberts flow I (Roberts 1972), which has been studied both analytically and through numerical simulations (Tilgner & Brandenburg 2008; Stasyszyn & Elstner 2015; Clarke et al. 2020), as well as the ABC flow (Teyssier et al. 2006; Bouya & Dormy 2012; Archontis et al. 2002; Baggaley et al. 2009). Convergence against the reference implementation in the Pencil Code (Pencil Code Collaboration et al. 2021) will be used to assess the correctness of our SPH solver. To ensure the validity of the results, MHD simulations are expected to maintain a solenoidal magnetic field. To monitor this, local divergence error metrics are used and corrective measures are employed. We study the impact of such measures on the growth of the magnetic field in these well-controlled experiments. The lessons learned from studying these flows allow us to construct an "over-winding" trigger detecting where the simulation's resolution is too low for a given kinematic dynamo to be properly resolved. This trigger can then be used in a cosmological setting to assess whether the geometry of the field in void regions is unaffected by numerical artefacts and could thus be used, in the future, to put constraints on the origin of the fields.

This paper is structured as follows. The codes, relevant differential equations and the error metrics are described in Sec. 2. The performance of our simulation code on the Roberts and ABC kinematic dynamo problems is presented in Sec. 3. The construction of the over-winding trigger and tests are presented in Sec. 4 with applications to a simple cosmological test case following in Sec. 5. Finally, in Sec. 6 we offer some conclusions and outlook on future applications of our code.

2 METHODS

In this section, we introduce the equations of MHD and their numerical implementations in the Swift (Sec. 2.2) and Pencil (Sec. 2.3) codes. We also introduce in Sec. 2.4 the error metrics we will use to monitor the divergence errors appearing in the code.

2.1 MHD

The evolution of magnetic field and plasma can be modeled using the MHD approximation (Widrow 2002; Brandenburg & Subramanian 2005):

$$\frac{\partial \mathbf{B}}{\partial t} = \mathrm{curl}[\mathbf{v} \times \mathbf{B}] + \eta \Delta \mathbf{B}, \tag{2}$$

$$\frac{\partial \mathbf{v}}{\partial t} + (\mathbf{v} \cdot \nabla)\mathbf{v} = -\frac{1}{\rho}\nabla P - \frac{1}{\rho}\nabla \mathbf{S} + \mathbf{\Pi}, \tag{3}$$

with $\mathbf{v}$ the fluid velocity, ρ the fluid density, $\mathbf{B}$ the magnetic flux density, η the physical resistivity, $\mathbf{S}$ the Maxwell stress tensor:

$$S_{ij} = \frac{1}{2}\frac{B^2}{\mu_0}\delta_{ij} - \frac{B_i B_j}{\mu_0}, \tag{4}$$

with μ_0 the vacuum permeability, and thermal pressure:

$$P = (\gamma - 1)\rho u \tag{5}$$

where u is the specific internal energy. The vector $\mathbf{\Pi}$ corresponds to an additional artificial viscosity and will be explained below. Additionally, there is an equation governing the specific energy density (see e.g. Price 2012):

$$\frac{\partial e}{\partial t} + (\mathbf{v} \cdot \nabla)e = -\frac{1}{\rho}\nabla_j v_i S_{ij} + \overline{\mathbf{\Pi}} \tag{6}$$

where $e = \mathbf{v}^2/2 + u + \mathbf{B}^2/2\rho$ is the specific energy density, $\overline{\mathbf{\Pi}}$ – energy dissipation term from viscous and resistive heating.

These equations describe the magnetic field, velocity and specific energy evolution as a function of spatial coordinates and time in the Eulerian frame.

2.2 MHD in the Swift code

The set of equations introduced above can be discretised in the Lagrangian frame using a particle-based approach within the framework of SPH (see e.g. Price 2012). More specifically, our implementation is built on top of the SPHENIX (Borrow et al. 2021) formulation of SPH that was designed specifically to perform well in galaxy formation simulations[1].

2.2.1 Momentum equation in SPH

We start with the discretisation of the momentum equation 3. The Swift code discretises the gas into a set of particles and solves the equations of motion at particle positions, i.e. in a frame where the observer moves with the fluid:

$$\frac{d\mathbf{v}}{dt} = -\frac{1}{\rho}\nabla \mathbf{S} + \mathbf{\Pi} + \mathbf{M} \tag{7}$$

with d/dt the material derivative, $\mathbf{\Pi}$ corresponding to additional artificial viscosity terms that help capture shocks at both hydrodynamic and magnetic wave discontinuities. This is achieved by using SPHENIX viscosity terms with a signal velocity that incorporates the Alfvén speed (Karapiperis et al. 2025). The term $\mathbf{M}$ is an additional force that corrects tensile instability akin to the Powell et al. (1999) term, an effective numerical force that arises due to the SPH discretisation and counteracts the particle clumping associated with $\frac{1}{\rho}\nabla S$. The magnitude of this effective force is proportional to the divergence of the magnetic field (Børve et al. 2001). The corrective term $\mathbf{M}$ explicitly violates energy conservation (Price 2012). The force becomes significant in regions where the magnetic pressure is comparable in magnitude to the thermal pressure. Consequently, maintaining a small divergence of the magnetic field is crucial to minimize both the particle-clumping component of $\frac{1}{\rho}\nabla S$ and the corrective term $\mathbf{M}$.

In SPH, the local matter density is computed as a sum:

$$\hat{\rho}_a = \sum_b m_b W(|\mathbf{r}_a - \mathbf{r}_b|, h_a), \tag{8}$$

where a and b are particle labels, W is the smoothing kernel and h the smoothing length, which is related to the local mean inter-particle separation.

The MHD momentum equation becomes

$$\frac{dv_a^i}{dt} = -\sum_b m_b \left[\frac{f_{ab} S_a^{ij}}{\hat{\rho}_a^2}\frac{\partial W_{ab}(h_a)}{\partial x_a^j} + \frac{f_{ba} S_b^{ij}}{\hat{\rho}_b^2}\frac{\partial W_{ab}(h_b)}{\partial x_b^j} \right] + \\ + \Pi_a^i + M_a^i + f_{\mathrm{grav}}^{a,i}, \tag{9}$$

where $f_{\mathrm{grav}}^{a,i}$ are the accelerations coming from gravity and f_{ab}:

$$f_{ab} = 1 + \frac{h_a}{3\hat{\rho}_a}\frac{\partial \hat{\rho}_a}{\partial h_a}. \tag{10}$$

are terms accounting for the spatial variation of the smoothing lengths. This set of equations is identical to the pure hydrodynamical case (see e.g. Price et al. 2018; Schaller et al. 2024) but with the pressure replaced by the Maxwell tensor and the tensile correction added.

2.2.2 Magnetic field evolution in SPH using direct induction

The simplest way to implement the evolution of the magnetic fields into SPH is to trace their evolution at particle positions:

$$\frac{d\mathbf{B}}{dt} = (\mathbf{B} \cdot \nabla)\mathbf{v} - \mathbf{B} \cdot \mathrm{div}\mathbf{v} + \eta \Delta \mathbf{B} + \Omega_{\mathrm{AR}} \tag{11}$$

with $\mathbf{v}$ the fluid particle velocity, Ω_{AR} an artificial resistivity corrective term to aid handling of magnetic field discontinuities (see e.g. Price 2012; Price et al. 2018).

Our direct induction (DI) implementation is fully described by Karapiperis et al. (2025). In summary, the equations of resistive MHD are solved by evolving the quantity $\mathbf{B}/\rho$, with $\mathbf{B}$ the magnetic flux density and ρ the mass density. The induction equation then reads:

$$\frac{d}{dt}\left(\frac{\mathbf{B}}{\rho}\right) = \left(\frac{\mathbf{B}}{\rho} \cdot \nabla\right)\mathbf{v} + \frac{\eta}{\rho}\Delta \mathbf{B} + \Omega_{\mathrm{AR}} - \frac{1}{\rho}\nabla \psi \tag{12}$$

with ψ a scalar field (the Dedner field), which is used to remove via hyperbolic and parabolic divergence cleaning any non-zero div$\mathbf{B}$ arising due to numerics (see e.g. Dedner et al. 2002; Tricco et al. 2016). The evolution equation for the scalar field itself is given by:

$$\frac{d}{dt}\left(\frac{\psi}{c_{\mathrm{h}}}\right) = -\sigma_{\mathrm{h}} c_{\mathrm{h}} \mathrm{div}\mathbf{B} - \frac{1}{2}\frac{\psi}{c_{\mathrm{h}}}\mathrm{div}\mathbf{v} - \sigma_{\mathrm{p}}\frac{\psi}{\tau_{\mathrm{c}}} \tag{13}$$

with c_{h} an appropriately chosen cleaning speed and τ_{c} is local Dedner scalar dissipation time:

$$c_{\mathrm{h}} = \sqrt{v_{\mathrm{A}}^2 + c_{\mathrm{S}}^2}, \qquad \tau_{\mathrm{c}} = \frac{h}{c_{\mathrm{h}}}, \qquad v_{\mathrm{A}} = \sqrt{B^2/(\mu_0 \rho)} \tag{14}$$

where σ_{h} and σ_{p} are constant parameters with typical values $\sigma \simeq 1.0$ (Price et al. 2018), v_{A} is the Alfvén speed and c_{S} the sound speed.

Several ways of expressing a divergence operator in SPH exist

[1] For completeness, all the runs employed version `3ea21e98` of the code.

(Price 2012). In our implementation of the cleaning terms, we choose the anti-symmetric divergence formulation:

$$\mathrm{div}\mathbf{B}_a = \frac{1}{\rho_a}\sum_b m_b(\mathbf{B}_b - \mathbf{B}_a)\cdot\nabla W_{ab}(h_a) \tag{15}$$

The discretised version of the induction equation then becomes (Karapiperis et al. 2025; Price et al. 2018):

$$\frac{d}{dt}\left(\frac{\mathbf{B}}{\rho}\right)_a = \Omega^a_{\mathrm{Str}} + \Omega^a_{\mathrm{Dender}} + \Omega^a_{\mathrm{Ohm}} + \Omega^a_{\mathrm{AR}} \tag{16}$$

with the stretching source term:

$$\Omega^a_{\mathrm{Str}} = -\frac{f_{ab}}{\hat{\rho}_a^2}\sum_b(\mathbf{v}_a - \mathbf{v}_b)(\mathbf{B}_a\cdot\nabla_a W_{ab}(h_a)) \tag{17}$$

divergence cleaning term:

$$\Omega^a_{\mathrm{Dender}} = -\sum_b m_b\left[\frac{f_{ab}\psi_a}{\hat{\rho}_a^2}\nabla_a W_{ab}(h_a) + \frac{f_{ba}\psi_b}{\hat{\rho}_b^2}\nabla_b W_{ab}(h_b)\right] \tag{18}$$

with the Ohmic (or physical) resistivity term:

$$\Omega^a_{\mathrm{Ohm}} = 2\eta\sum_b m_b\frac{\partial_{\mathrm{r}}W_{ab}(h_a)}{|r_{ab}|\hat{\rho}_a\hat{\rho}_b}(\mathbf{B}_a - \mathbf{B}_b). \tag{19}$$

Note that our implementation also uses artificial resistivity terms but these were switched off in what follows as we are concerned with the precise effect of physical Ohmic resistivity alone.

2.2.3 *Vector Potential (VP) MHD implementation in Swift*

Alternatively, the magnetic field divergence constraint can be enforced by evolving for the vector potential (VP; Stasyszyn & Elstner 2015) instead of the magnetic field. The magnetic field in terms of the vector potential $\mathbf{A}$ is then:

$$\mathbf{B} = \mathrm{curl}\mathbf{A}. \tag{20}$$

The induction equation for $\mathbf{A}$ reads:

$$\frac{d}{dt}\mathbf{A} = \mathbf{v}\times\mathrm{curl}\mathbf{A} + (\mathbf{v}\cdot\nabla)\mathbf{A} + \eta\Delta\mathbf{A} - \nabla\Gamma, \tag{21}$$

where Γ is the electromagnetic gauge. The gauge does not influence the magnetic field and only governs the evolution of the vector potential. Since Maxwell's equations, when expressed in terms of the vector potential, do not uniquely determine it, a gauge condition must be chosen (Jackson 1999). One possible choice is the Coulomb gauge, where $\mathrm{div}\mathbf{A} = 0$. To enforce this condition numerically, a new scalar field can be introduced, sourced by the residual $\mathrm{div}\mathbf{A}$ (Stasyszyn et al. 2012). Similarly to Dedner divergence cleaning, the electromagnetic gauge Γ propagates and removes the divergence of the $\mathbf{A}$ field through its evolution equation:

$$\frac{d}{dt}\Gamma = -c_{\mathrm{h}}^2(\nabla\cdot\mathbf{A}) - \frac{c_{\mathrm{h}}^2}{\tau_{\mathrm{c}}}\Gamma, \tag{22}$$

where c_{h},τ_{c} defined the same way as for Dedner cleaning (Eq. 14). The SPH version of the induction equation for vector potential then reads:

$$\frac{d}{dt}\mathbf{A}_a = \Omega^a_{\mathrm{Str}} + \Omega^a_{\mathrm{Gauge}} + \Omega^a_{\mathrm{Ohm}} \tag{23}$$

with stretching term:

$$\Omega^a_{\mathrm{Str}} = \frac{f_{ab}}{\hat{\rho}_a}\sum_b m_b(\mathbf{v}_a - \mathbf{v}_b)\mathbf{A}_a\nabla_a W_{ab}(h_a) \tag{24}$$

gauge term

$$\Omega^a_{\mathrm{Gauge}} = \frac{f_{ab}}{\hat{\rho}_a}\sum_b m_b(\Gamma_a - \Gamma_b)\nabla_a W_{ab}(h_a) \tag{25}$$

with the observed B field reading:

$$\mathbf{B}_a = \sum_b\frac{m_b}{\hat{\rho}_b}(\mathbf{A}_a - \mathbf{A}_b)\times\nabla_a W_{ab}(h_a)). \tag{26}$$

As was the case for the direct induction method, we add an Ohmic resistivity term which, here, acts directly on $\mathbf{A}$:

$$\Omega^a_{\mathrm{Ohm}} = 2\eta\sum_b\frac{m_b\hat{\rho}_a}{|r_{ab}|\hat{\rho}^2_{ab}}\frac{\partial_{\mathrm{r}}W_{ab}(h_a) + \partial_{\mathrm{r}}W_{ab}(h_b)}{2}(\mathbf{A}_a - \mathbf{A}_b), \tag{27}$$

where $\hat{\rho}_{ab} = \frac{1}{2}(\hat{\rho}_a + \hat{\rho}_b)$.

In what follows, we will make use of both flavours of SPMHD with special attention to the direct induction scheme.

2.3 MHD in the Pencil Code

As mentioned above, we make use of the Pencil code (Brandenburg & Dobler 2002; Brandenburg 2003), a thoroughly tested and validated grid code, as a reference against which to evaluate performance of Swift's MHD implementations.

In the Pencil Code, space is divided into a grid of fixed points. Spatial derivatives are calculated as combination of values of a function at the point and its neighbours in the direction of derivative using centered finite differences approach:

$$f_i' = (-f_{i-3} + 9f_{i-2} - 45f_{i-1} + 45f_{i+1} - 9f_{i+2} + f_{i+3})/(60\delta x), \tag{28}$$

$$f_i'' = (2f_{i-3} - 27f_{i-2} + 270f_{i-1} - 490f_i + \\ + 270f_{i+1} - 27f_{i+2} + 2f_{i+3})/(180\delta x^2). \tag{29}$$

For time integration the third order $2N$-Runge-Kutta scheme is used (Williamson 1980).

The equations for density and velocity fields in the Eulerian frame:

$$\frac{\partial}{\partial t}\ln\rho + (\mathbf{v}\cdot\nabla)\ln\rho = -\mathrm{div}\mathbf{v}, \tag{30}$$

$$\frac{\partial}{\partial t}\mathbf{v} + (\mathbf{v}\cdot\nabla)\mathbf{v} = -\frac{\nabla P}{\rho} + \ln\rho + \frac{1}{\rho}\mathbf{J}\times\mathbf{B} + \mathbf{f}_{\mathrm{visc}} + \mathbf{f}_{\mathrm{grav}}, \tag{31}$$

where $\mathbf{f}_{\mathrm{visc}}$ is the viscous force per unit mass, which is proportional to the viscosity ν and the divergence of the traceless rate-of-strain tensor. The magnetic field equations are solved using the vector potential in the Weyl gauge ($\Gamma = 0$) in an Eulerian frame:

$$\frac{\partial\mathbf{A}}{\partial t} = \mathbf{u}\times\nabla\times\mathbf{A} + \eta\nabla^2\mathbf{A}. \tag{32}$$

To deal with discontinuities and discretization errors the code involves some non-zero ν and η in Eqs. (31) and (32) using a high-order spatial discretisation as in Eqs. (28) and (29). For the kinematic dynamo problems such as Roberts Flow I, the momentum equation is not solved explicitly. Instead the velocity field is given as a coordinate-dependent function. For internal energy the isothermal equation of state was used.

2.4 Magnetic field error metrics in Swift

In a direction induction method, magnetic field evolution divergence errors can occur due to numerical errors. Even though the Dedner

cleaning scheme acts to reduce the divergence, it is useful to have a set of tools to monitor the spurious monopole component of the magnetic fields. We introduce the ones we use here.

The most widely used error metric for SPMHD is the ratio (e.g. Eq. (78) of Price & Monaghan 2005):

$$R_{0,a} = \frac{|\mathrm{div}\mathbf{B}_a| \cdot h_a}{|\mathbf{B}_a|}. \tag{33}$$

Whilst directly related to the problem we want to monitor and to the term sourcing the Dedner scalar evolution, this error metric is large only if the divergence is of order of largest resolvable gradient by SPH, $\sim |\mathbf{B}_a|/h_a$ (see below).

In addition, the outcomes of divergence presence are not limited to some unphysical field fraction in the magnetic field, and thus require additional monitoring techniques. If the error metric R_0 is small, it does not guarantee that the effect of the spurious divergence is small. For example, there are monopole forces proportional to div**B** that could result in major forces affecting the dynamics of a particle. To monitor such situations, another, more rarely used metric monitors the component of the magnetic field that is parallel to the total magnetic force acting on the fluid (see Eq. (79) of Price & Monaghan 2005). It thus is a spurious force:

$$R_{1,a} = \frac{(\mathbf{B}_a \cdot \mathbf{f}_{\mathrm{mag},a})}{|\mathbf{B}_a||\mathbf{f}_{\mathrm{mag},a}|}, \tag{34}$$

where $\mathbf{f}_{\mathrm{mag},a}$ is the sum of the first term corresponding to $-\frac{1}{\rho}\nabla S$ in Eq. (9) and the monopole correction force $\mathbf{M}_a$.

Finally, even when magnetic forces parallel to the magnetic field are small (i.e. R_1 is small), the monopole component of the magnetic field can create an additional spurious Lorentz force. To monitor this, one can estimate the magnitude of the monopole component relative to the physical magnetic field. To this end, we introduce the ratio of the magnetic field divergence to the current:

$$R_{2,a} = \frac{|\mathrm{div}\mathbf{B}_a|}{|\mathrm{curl}\mathbf{B}_a|}. \tag{35}$$

All these error metrics can be large in regions where the values of the div$\mathbf{B}_a$ and curl$\mathbf{B}_a$ operators are very sensitive to the particle arrangement. The particle noise level can be conservatively estimated as the level of error of the SPH gradient operator (e.g. Price 2012; Violeau 2015). Assigning a unity scalar quantity to SPH gas particles and computing a gradient vector, which in the continuum limit should be zero, yields:

$$\langle \nabla 1 \rangle_a = \sum_b \frac{m_b}{\hat{\rho}_b} \nabla W(|\mathbf{r} - \mathbf{r}_b|, h(\mathbf{r}))\Big|_{\mathbf{r}=\mathbf{r}_a}. \tag{36}$$

This quantity will be non-zero due to particle arrangement in space. Using this construction, the errors induced by particle noise in the divergence and curl operators can be estimated as:

$$\begin{aligned}
\langle \delta \mathrm{div}\mathbf{B}_a \rangle &\simeq (\langle \nabla 1 \rangle_a \cdot \mathbf{B}_a), \\
\langle \delta \mathrm{curl}\mathbf{B}_a \rangle &\simeq [\langle \nabla 1 \rangle_a \times \mathbf{B}_a], \\
\langle \delta \mathbf{f}_{\mathrm{mag},a} \rangle &\simeq \frac{S_a^{ii}}{3\hat{\rho}_a} \cdot \langle \nabla 1 \rangle_a.
\end{aligned} \tag{37}$$

In what follows, and more generally in Swift, when measuring the three error metrics introduced above, we explicitly zero the quantities that are not 10× larger than their corresponding pure-noise counterparts. This allows us to focus our analysis on regions where the errors are not triggering solely due to the noise in the particle distribution. Note however that the Dedner evolution equation (13) does not use this limit; any (spurious) div**B** appearing in the fluid is sourcing the scalar field evolution.

3 KINEMATIC DYNAMO TESTS

Dynamos are crucial for cosmological and astrophysical magnetic field evolution. Therefore, correctly capturing the amplification process is a necessary step in the validation of a numerical code. In this section we study the performance and limitations of the SPMHD implementations in Swift code introduced above on the standard Roberts (1972) flow and the Arnold–Beltrami–Childress (ABC; Arnold 2014; Childress 1970) flow dynamo test problems. Both of these tests probe the kinematic dynamo regime.

The main aim of these test is to verify that the induction source term together with resistive terms in the code are modelled correctly and allow correct reproduction of magnetic field growth. In particular, we focus on characteristics such as the growth rate dependence on the physical resistivity and resolution convergence as well as on qualitative features such as the spacial magnetic field distribution and the mode transitions. We compare our results to the Pencil code and to published solutions.

3.1 The Roberts flow I test

There are several simple dynamo capable flows consisting of four vortices in the xy-plane with a uniform velocity field in the z direction (Roberts 1972). These flow problems have been widely studied both with simulations and semi-analytically. The different flows proposed in this paper vary in their $v_z(x, y)$ dependence and provide a range of mechanisms for magnetic field growth. One of them, the first flow, exhibits growth via the alpha effect (Tilgner & Brandenburg 2008). Flows II and III show growth due to a memory effect (Rheinhardt et al. 2014). The fourth flow provides growth through effective negative turbulent diffusivity (Devlen et al. 2013).

The first flow was chosen for our study for its simplicity and relevance to cosmology and astrophysics since it manifests the alpha effect, which is important in galaxy disks (e.g. Widrow 2002; Brandenburg & Ntormousi 2023).

To test the induction in the Swift code, the kinematic dynamo regime was chosen. This is the regime where the velocity field is not affected by the back-reaction from the magnetic field via the Lorentz force. This renders the equations linear and allows different modes (sourced in the initial conditions) to grow independently. On the code level we force the particles to obey at all times the following velocity vectors:

$$\mathbf{v}_a = \mathbf{v}_\mathrm{f}(\mathbf{r}_a). \tag{38}$$

where $\mathbf{v}_\mathrm{f}$ is the forcing velocity field given below.

3.1.1 *Detailed setup*

For the velocity field of the flow, we use the same convention as Rheinhardt et al. (2014):

$$\begin{aligned}
v_{\mathrm{f},x} &= v_0 \sin k_0 x \cos k_0 y \\
v_{\mathrm{f},y} &= -v_0 \cos k_0 x \sin k_0 y \\
v_{\mathrm{f},z} &= \omega_0 \sin k_0 x \sin k_0 y
\end{aligned}$$

where $v_{\mathrm{f},i}$ are the components of the particle velocity, x, y, z the particle positions, and v_0, ω_0 the magnitudes of the planar and vertical velocities respectively. In our configuration, we fix $k_0 = 2\pi/L_\mathrm{box} = 1$ and $\omega_0/\sqrt{2} = v_0 = 1$ such that the spread in velocities is normalised $v_\mathrm{rms} = 1$.

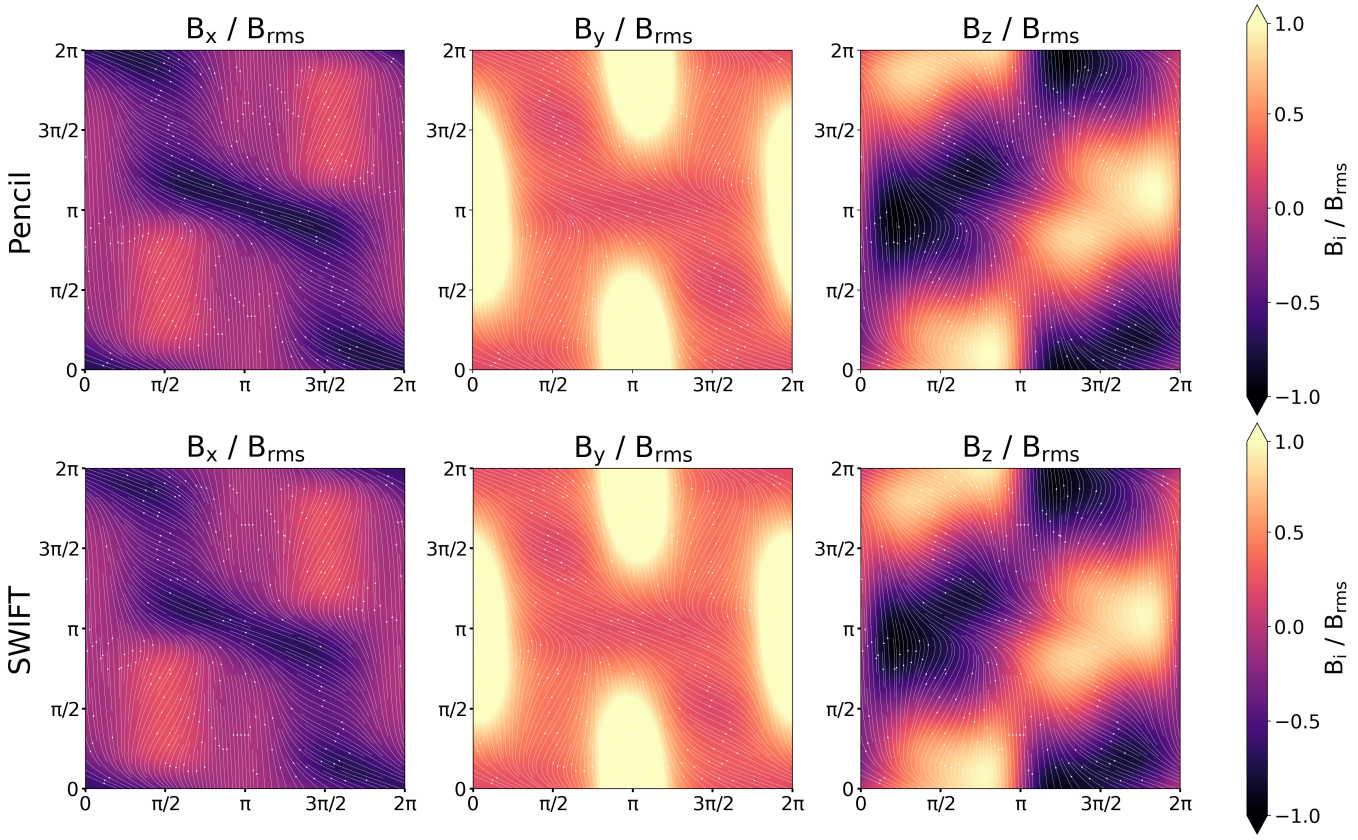

Figure 1. Maps of the magnetic field components B_x (left), B_y (middle), and B_z in units of the magnetic field RMS in the xy-plane at $z = 0.0$ for Pencil and $z = 0.05$ for Swift (for explanation of such choice see text) at around $t > 20$ using the direct induction scheme (bottom row) with $N = 32^3$ particles. The white streamlines indicate the magnetic fields inside the plane. The growing mode of the magnetic fields in Swift reproduces well the observed features in the fields extracted from the Pencil code.

For the magnetic fields, we use three separate initial configurations:
First, *random initial conditions (ICs)*: We generate a uniform distribution of vector potentials $\mathbf{A}$ with random length in range $[0,A_0]$. While initially the vector potential is not smooth, the magnetic field is calculated through SPH version of the equation $\mathbf{B} = \mathrm{curl}\mathbf{A}$ (Eq. 20) is spatially smooth and divergence-less form of $\vec{B}$ by construction.
Second, *random ICs without bulk MF*: calculation of the magnetic field from random vector potential may introduce a small constant field component. Such components along the z direction will not decay, and thus can influence decaying modes (see Sec. 3.2 below). Thus, the volume averaged magnetic field is subtracted.
Third, we employ a *Beltrami-type field*, i.e. a field for which the relation $\mathrm{curl}\mathbf{B} = k\mathbf{B}$ holds, which is also divergence-less. More specifically, we use:

$$\begin{aligned} B_x &= B_0(\sin ky + \sin kz),\\ B_y &= B_0(\cos kx - \cos kz),\\ B_z &= B_0(\sin kx + \cos ky). \end{aligned} \tag{39}$$

The constants B_0, A_0 are the magnetic field and vector potential normalization factors respectively. Setting the magnetic field wavenumber to $k = 1$ was enough to start the mode with the largest growth rate in the range $\eta \in [0.1, 0.2]$ (see Sec. 3.2 below). We set the initial field B_0 or A_0 such that $B_{\mathrm{rms}}(t = 0) = 10^{-4}B_{\mathrm{eq}}$, where equipartition estimate is:

$$\epsilon_{\mathrm{mag}} \simeq \epsilon_{\mathrm{kin}}, \qquad \epsilon_{\mathrm{mag}} = \frac{B_{\mathrm{eq}}^2}{2\mu_0}, \qquad \epsilon_{\mathrm{kin}} = \frac{v_{\mathrm{rms}}^2}{2}, \tag{40}$$

where $k = 2\pi/L$ for our domain of size L^3.

As mentioned above, we make use of Eq. (1) for the magnetic Reynolds number definition. For completeness, we chose a value of the internal energy, u, of order 1000 such that the resulting flow remains sub-sonic at all times. Note that, in this setup, the sound speed only affects the time-step size (via the Courant condition) and the Dedener cleaning speed.

3.1.2 *Qualitative Roberts flow I results*

We study the Roberts flow I problem using 16^3, 24^3, 32^3, 48^3, 64^3 and 128^3 particles initially arranged in a glass-like (random) setup with uniform density[2].

To ensure that Swift correctly reproduces Roberts flows, we expect the magnetic field distribution, $\mathbf{B}(x, y, z)$, across the simulation volume to be comparable to that obtained from other MHD codes. While

[2] A glass arrangement can be obtained by starting with particles in a cubic grid lattice with small perturbations in lattice positions, with no pressure gradients or velocities and by letting particles move under numerical forces to a configuration where the kinetic energy does not change any more.

the amplitude of the magnetic field in a growing mode increases exponentially with time, its normalized spatial distribution—given by $\mathbf{B}(x, y, z, t)/B_{\rm rms}(t)$ —should remain time-independent.

For code comparison, we use data from a Roberts flow simulation performed with the Pencil Code. This simulation follows the setup described above, initialized with a random vector potential at a physical resistivity around $\eta \simeq 0.18$. Since Roberts flows exhibit translational symmetry along the z direction, a growing mode initialized with random conditions can manifest with an arbitrary shift along z. To eliminate this ambiguity in the Swift simulations, we opted for a single-mode initial condition (Eq. 39), which ensures that the growing mode appears without an arbitrary vertical shift.

Figure 1 compares the spatial configuration of the magnetic field components between Swift and Pencil Code runs. The upper row displays the magnetic field distribution in a 32^3 - resolution Pencil Code simulation, taken as a grid cell values at $z = 0$. The lower row presents results from a 32^3 - resolution Swift run, sliced at $z = 0.05\,L_{\rm box}$. In both cases, the plots show density maps of the individual magnetic field components, normalized by the root mean square magnetic field over the simulation volume. The visual agreement between the two codes indicates that Swift's direct induction MHD implementation accurately reproduces the expected field configuration, demonstrating consistency with the Pencil Code results. We also verified that the vector potential implementation leads to similar results.

Having verified that our SPMHD implementation agrees qualitatively with the reference implementation in the Pencil Code, we move on to quantitative measurements of the growth rate of the field.

3.2 Growth rate comparison

The instantaneous growth rate, γ_i , is defined as:

$$\gamma_i = \frac{d}{dt}\ln(B_{\rm rms}), \tag{41}$$

where $B_{\rm rms}$ is the root-mean-square average of the B-field in the whole simulation volume. The instantaneous growth rate is averaged on the interval where it is roughly constant. For our runs, specifically, we choose to measure quantities at an interval $\delta t = 0.05$ in internal time units over the range $t \in [30, 70]$, where the growth rate is indeed well-behaved and constant. The growth rate and fluctuations are then calculated as:

$$\gamma = \langle\gamma_i\rangle_{\rm t}, \qquad \delta\gamma = 2 \cdot \sqrt{\langle(\gamma_i - \gamma)^2\rangle_{\rm t}}. \tag{42}$$

In the Roberts flow setup, the excited magnetic field mode grows exponentially with time and has a growth rate that depends directly the magnetic Reynolds number. In our experiments, the velocity and wavelength of the flow are fixed and the physical resistivity is varied in order to change $R_{\rm m}$. We report the resulting dependence of the growth rate on the resistivity in Fig. 2. The top panel depicts the growth rate as a function of resistivity near the dynamo onset, while the bottom panel illustrates its behavior in the ideal MHD limit ($\eta \to 0$). Note that the x-axis in the bottom panel is log-scaled for resistivity. The black line represents results from Pencil code simulations at a 32^3 resolution, whereas the red and blue lines correspond to the DI and VP MHD implementations in Swift code at 64^3 resolution. In the Pencil Code, random ICs were used for all data points. For the Swift code, random ICs were applied for $\eta < 0.1$, while one-mode ICs were used for $\eta \sim [0.1, 0.2]$. The top panel shows growth rate as a function of resistivity near the dynamo onset. The bottom panel illustrates how the growth rate behaves in the ideal MHD limit, $\eta \to 0$ (note that for the bottom panel, the x axis shows the log scaled resistivity). Black line shows 32^3 Pencil code runs, red and blue show DI and VP MHD implementations in Swift code at 64^3 resolution. The random ICs were used for Pencil code for all points, while for Swift code the random ICs were used for $\eta < 0.1$ and one-mode ICs for $\eta \in [0.1, 0.2]$. Both MHD flavors in Swift exhibit slightly lower growth rates compared to the reference results from the Pencil code. However, both SPMHD implementations accurately capture the overall relationship between γ and η for high resistivity. The VP scheme underestimates growth rates relative to the DI scheme. One possible explanation is that, in the version of the code used for this study, parameters in the gauge equation were not as well optimized for the VP implementation as they were for the cleaning in DI.

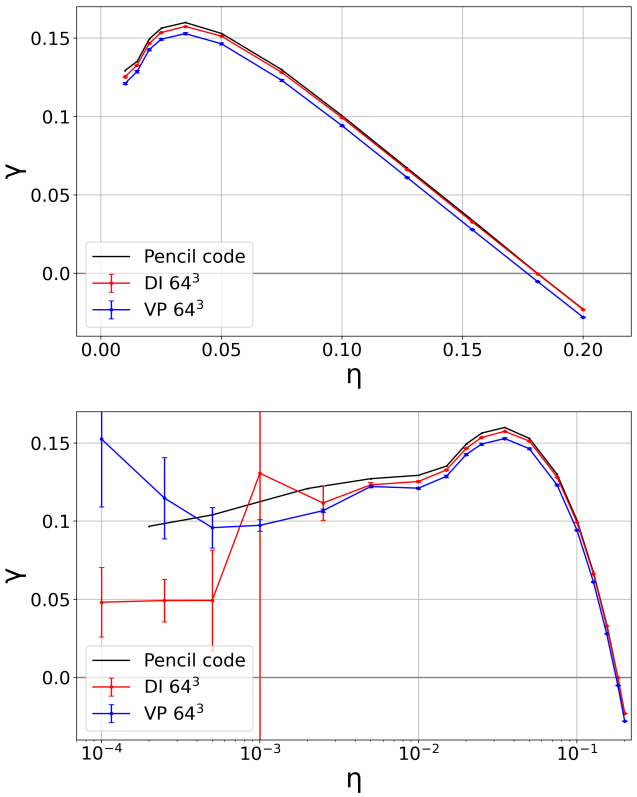

Figure 2. Top panel: The growth rate of the Roberts Flow 1 dynamo as a function of the physical Ohmic resistivity for the Pencil code with 32^3 cells (black line) compared to both Swift MHD implementations using 64^3 particles (red, blue). The bottom panel shows the same data but using a logarithmic axis for the resistivity to focus on the behaviour of the growth rates close to the ideal MHD limit ($\eta \to 0$). Negative growth rates indicate decaying modes. The error bars represent the magnitude of numerical growth rate fluctuations. The direct induction (DI, red curve) implementation of SPMHD in Swift matches the Pencil Code results closely for almost all values of the resistivity (and thus Reynolds number); the cross-over point between growing and decaying modes, in particular, matches precisely. Deviations are only found close to the ideal MHD limit. The vector potential (VP, blue curve) implementation displays a systematically lower growth rate than the other models.

The errors in Eq. (20) probably do not influence the measurement of magnetic field growth since the spacial distribution of vector potential is time independent for a growing mode, such that $\mathbf{A}(x, y, z, t) = f(t)\mathbf{A}(x, y, z)$.

The lower resolution runs, 32^3 and 16^3 exhibit the same behavior, but the deviation from the Pencil code is larger for smaller

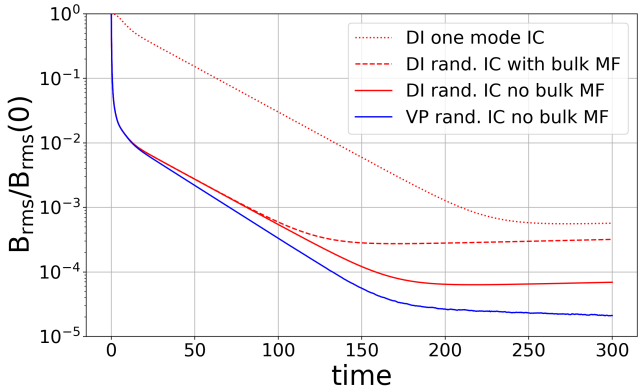

Figure 3. Magnetic field time evolution for decaying mode with different ICs: with one specific mode excited (red, dotted line), with random initial magnetic without bulk magnetic field subtraction (red, dashed line), with random magnetic field with bulk field subtracted (solid red - DI, solid blue - VP). The single-mode ICs consist of a Beltrami field with wavelength $\lambda = L_{\rm box}$. For all of the runs the correct decaying mode appears initially, but for DI is followed by other, slowly growing mode and slowly decaying modes. The runs indicate that longevity of the decaying mode can be improved by bulk field subtraction. However, the longer time behavior is not connected to the bulk field subtraction. Since one-mode ICs provide the longest existence time for the decaying mode, this initial field configuration was chosen to study the dynamo onset resistivity in what follows.

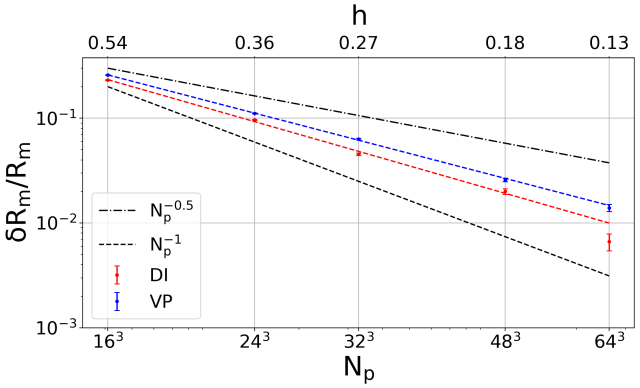

Figure 4. Relative deviation of the critical Reynolds magnetic number of the Roberts flow I problem from the one extracted from our highest-resolution ($N = 128^3$ particles) as a function of the number of particles (bottom axis), or smoothing length (top axis) in a simulation of size $L_{\rm box} = 2\pi$. The black lines indicate slopes of $N^{-0.5}$ and N^{-1}. Both MHD implementations in Swift converge with increasing resolution at a relatively similar rate.

resolutions.

The limit of small physical resistivity is crucial for the future Swift applications to cosmology and astrophysics since it translates to large ($R_m \gtrsim 10 \sim 100$) magnetic Reynolds number. In the Roberts flow I case, when decreasing the resistivity down to $\eta \simeq 3 \cdot 10^{-3}$ (i.e $R_{\rm m} \simeq 300$), the growth rate deviation of the SPMHD implementations from the Pencil code increases (bottom panel of Fig. 2). For our runs, the growth rate is not the same and shows some resolution-dependent fluctuations. These fluctuations are illustrated as error bars on the figure where we used 2 standard deviations as the size of the bar. For growing mode solutions, the relative magnitude of the growth rate uncertainty is at the level of 10^{-2} but increases for lower resistivity and for lower resolution. At $\eta \simeq 10^{-3}$–10^{-4} (or $R_{\rm m} = 1000$–10000) the growth rate fluctuations become of the same order as the growth rate itself.

Focusing now on the last two points from the right, (i.e. $\eta = 0.1811, 0.2$), from Fig. 2, the decaying mode forms, as expected. Our experiments show, however, that if the random ICs (rather than the Beltrami field) are used the negative growth rate does not become constant with time and slowly tends to zero with the magnetic field reaching some plateau and only slowly changing with time. This behaviour is highlighted on Fig. 3 where we tested both MHD implementations and and three types of initial conditions for the DI case:

- random magnetic field with bulk field subtracted,
- random magnetic field without bulk field subtraction,
- single-mode ICs, i.e. Beltrami field.

For all schemes and ICs, the decay stops. But with one-mode ICs the decaying modes exist for a more extended period of time, which helps the precise measurement of the growth or decay rate. We thus use such single-mode ICs in the following precision tests, in range $\eta \sim [0.1, 0.2]$. For small resistivity, $\eta \to 0$, the modes with $k <$ 1 become important (e.g. Roberts 1972). For this reason we used random ICs in $\eta < 0.1$, because they contain a spectrum of modes, with wavelength spanning from resolution scale up to the simulation boxsize.

3.3 Transition from growing to decaying regime

An important aspect is the dynamo onset resistivity and the corresponding $R_{\rm m}$. This is the critical resistivity at which the behaviour transition from a growing to a decaying magnetic field. If captured incorrectly by an implementation, kinetic dynamos can appear under incorrect conditions. In the case of more complex simulations such as cosmological MHD simulations this can result too much or too little magnetic field growth and can be harder to identify than for less complex systems. The cosmological simulations can also have some resolved and under resolved flows, and the resolution dependence of critical magnetic Reynolds number $R_{\rm m}^{\rm crit}$ in the Roberts Flow I test can thus give us insight to the dependence of the dynamo strength on the flow resolution in different regions of cosmological simulations. Tilgner & Brandenburg (2008) measured the transition from decaying to growing modes in the Roberts flow I test to occur around $R_{\rm m}^{\rm crit} \simeq 5.52$, which corresponds to $\eta = 0.1811$ for the setup. The results of the simulations are resolution dependent, but we should expect them to converge to the correct $R_{\rm m}^{\rm crit}$. To validate the implementations and obtain their convergence rates, we started by running a series of additional simulations using 128^3 particles around the expected critical resistivity. We then measure the growth rate and interpolate between the measured values to get $R_{\rm m}^{\rm crit}$. Using this procedure, we find:

$$R_{\rm m}^{\rm crit} = 5.487 \pm 0.005 \qquad \text{(DI implementation)},$$
$$R_{\rm m}^{\rm crit} = 5.571 \pm 0.004 \qquad \text{(VP implementation)},$$

in reasonable agreement with published values.

To study the convergence rate, we repeat the same exercise but using simulations with 16^3, 24^3, 32^3, 48^3, and 64^3 particles. We then measure the difference between the critical resistivity obtained at a given resolution and the value extracted from our highest resolution run (reported above). This difference is shown in Fig. 4 as a function of the particle number (bottom axis) or, equivalently, as a function of

the SPH smoothing scale, i.e. the spatial resolution (top axis). As can be seen, both schemes do converge to the solution though at slightly different rates. We additionally measure the convergence rate as a function of particle number by fitting a power law to the data on the figure. We find slopes of:

$$\alpha = -0.762 \pm 0.023 \qquad \text{(DI implementation)},$$
$$\alpha = -0.690 \pm 0.014 \qquad \text{(VP implementation)},$$

i.e. a convergence rate close to second order in the spatial resolution ($\delta R_{\rm m} \propto h^2$).

3.4 Impact of resolution and resistivity

Magnetic field pattern develops thinner features as the resistivity decreases. At some threshold resistivity and resolution, distortions of the magnetic patterns appear. However, for higher resolution, at fixed η, the distortions are absent, indicating the connection of magnetic field pattern breakdown in the ideal MHD limit and resolution. The process of increasing resolution at a fixed resistivity is visually illustrated in the left three panels of Fig. 5. The figure presents density maps of magnetic field slices, depicting $B_y(x, y, z, t)/B_{\rm rms}(t)$ in the xy-plane for resolutions of 16^3, 32^3, and 64^3 at $\eta = 0.01$, along with a 64^3 run without resistivity. In all cases, random initial conditions were used, and the slice heights were adjusted to capture the same feature. The colormaps represent the magnitude of the magnetic field component, using the same color scale as in Figure 1. White streamlines indicate magnetic field lines in the xy-plane.

As the resolution increases from left to right, initially unresolved structures reveal more detail, reducing blob-like distortions. However, in the zero-resistivity case, the pattern remains distorted at all resolutions, with elevated magnetic field regions appearing along the vortex boundaries ($x = \pi n$ and $y = \pi m$, where n, m are integers), with a characteristic size on the order of the resolution scale (Figure 5, rightmost plot). The growth of magnetic distortions at the resolution scale in the absence of resistivity is not unique to the Swift DI or VP implementations and has also been observed in other MHD dynamo simulations (e.g. Brandenburg 2010).

3.5 Influence of spurious magnetic field divergence

Physical magnetic field should maintain the solenoidality condition ($\mathrm{div}\mathbf{B} = 0$). Probing the level of spurious divergence can help indicate how much the simulation results can be trusted. The velocity field forcing term used for the Roberts flow test decouples the force equation from the induction one. As such, the only way spurious divergence can affect the magnetic field evolution is through the induction equation. Ideally, in the Eulerian frame, the induction term $\mathrm{curl}[\mathbf{v} \times \mathbf{B}]$ should not generate any divergence. However, due to inaccuracies in the SPH operator, the induction term may inadvertently introduce divergence. The presence of a monopole component in the magnetic field, $\mathbf{B}_{\rm mon}$, can then act as a source for physical fields through the term $\mathrm{curl}[\mathbf{v} \times \mathbf{B}_{\rm mon}]$, potentially altering the magnetic field growth rate.

As an initial check, we monitored the mean divergence error throughout our runs. The divergence was evaluated once the growing mode was established, using a time-averaged measurement over the interval $t \in [30, 70]$ and with volume-averaging over the entire simulation domain. The results are reported as a function of resistivity on Fig. 6. The figure presents the divergence error, R_0, without noise cancellation for 64^3 DI and VP runs. Now we also include the direct induction runs with measures to clean the divergence (Sec. 2.2.2). For resistivity values above $\eta \simeq 3 \times 10^{-3}$, magnetic field is well behaved, the error remains below 10% in all cases. However, for smaller resistivity, the errors increase significantly. In the VP runs, the error saturates at approximately 20%. In DI runs without cleaning, the error continues to grow as resistivity decreases until a significant portion of the field consists of monopole component. When Dedner cleaning is enabled, the errors are significantly reduced to an acceptable level of about 5%, and exhibit behavior more similar to VP. The DI implementation with cleaning results less errors than VP over whole resistivity range.

In addition to monitoring global averages, it is also instructive to examine the spatial distribution of divergence errors. We used two error metrics introduced in Sec.2.4: R_0 and R_2. Colormaps of these error metrics for Roberts Flow I at $\eta = 0.01$ (where pattern destruction occurs for $N = 16^3$ particles; see below) are shown in Fig.7 for three different resolutions, along with an additional run in the ideal MHD limit. All runs were performed using the DI implementation with divergence cleaning enabled. These maps correspond to the same setup and time as those in Fig. 5.

The mean errors remain small across the simulation volume for all resolutions but are more pronounced inside vortices, that correlates with large shear in the velocity of the Roberts flow. The R_2 metric highlights similar regions as R_0 but tends to yield slightly lower values. In the ideal MHD case (i.e., zero resistivity), the R_0 metric remains mostly below 10%, whereas R_2 exceeds 10%. This indicates that the two error metrics are not entirely equivalent, and R_0 alone does not fully capture all unphysical magnetic field.

The Roberts flow I is an idealized setup where the divergence can remain low both in space and time, and particle distributions, along with other quantities, are smooth. However, in real astrophysical and cosmological simulations, strong density, magnetic field, and velocity contrasts exist, and the particle distribution is highly non-uniform. Additionally, processes such as energy injection from subgrid models and particle removal can introduce sudden spikes in divergence. Therefore, it is crucial to investigate the impact of large divergence errors on the growth rate, evaluate the effectiveness and determine the main source of divergence cleaning.

To assess the cleaning performance in a dynamo setting, we conducted additional runs in which a large divergence error was deliberately introduced in the initial conditions. This was achieved by generating random initial conditions similar to ones described in Sec. 3.1, but with randomly oriented **B** field vectors instead of random **A**, thereby ensuring a significant monopole component in the magnetic field.

Figure 8 illustrates the evolution of the magnetic field and divergence error over time for the DI implementation. Initially, divergence cleaning was disabled (yellow lines), and we observed that physical resistivity alone was sufficient to dissipate the large initial divergence error. However, when divergence cleaning was enabled, the errors were removed much more rapidly (brown lines). Ultimately, the divergence error saturated at the same level as in runs with divergence-free (random ICs from Sec. 3.1) initial conditions (green lines).

Thus, while some error reduction occurs naturally due to the resistivity term, the Dedner cleaning terms provide a significantly more effective correction.

The growth rates of growing modes (solid lines) remained unaffected by the divergence cleaning. However, for decaying modes (dashed lines), the run with resistivity alone exhibited a slightly slower decay compared to the runs with Dedner cleaning, suggesting the presence of a small additional diffusion effect from the cleaning process.

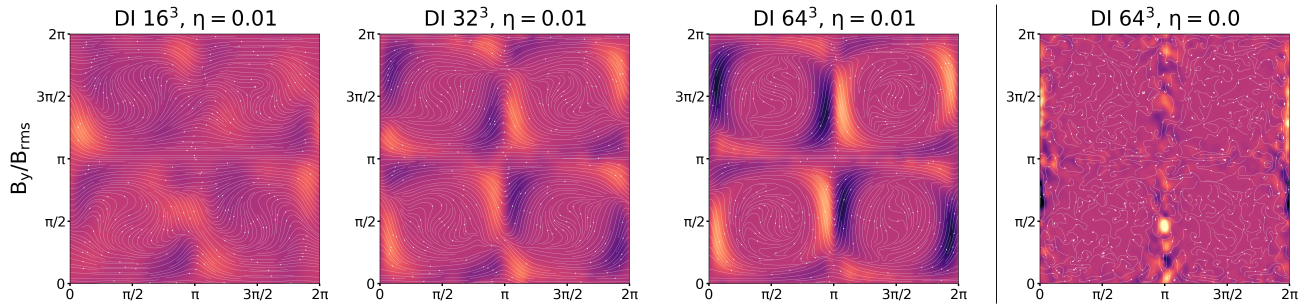

Figure 5. Colormaps for $B_y/B_{\rm rms}$ at $t = 50$ in XY plane for Roberts Flow 1 runs at 16^3 (left), 32^3 (center left), 64^3 (center right) resolution with $\eta = 0.01$ and $\eta = 0$ run at 64^3 (right). For low resolution runs magnetic field pattern appears more distorted than at higher resolution. As the resolution is increased more thin magnetic field features become visible. In the limit of zero resistivity, the magnetic field pattern becomes unresolved for any resolution.

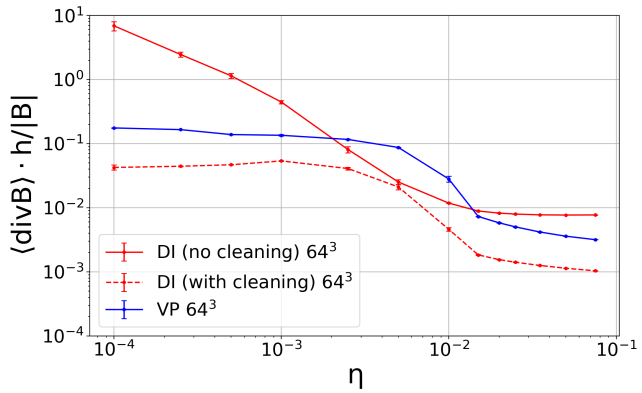

Figure 6. Magnitude of mean volume and time averaged divergence error vs physical resistivity for 64^3 runs for Swift MHD implementations. The divergence errors here for both DI and VP are the measure of accuracy of the produced B field. For DI the divergence is also entering equations of motion. The error experiences order of magnitude jump around $\eta \sim 3 \cdot 10^{-3}$ for both MHD implementations in the same region where large growth rate deviations from Pencil code appear. For direct induction scheme the Dedner cleaning helps to keep divergence errors where otherwise they will be big (red solid and dashed lines).

3.6 The ABC flow

Before closing this section on classical dyanmo tests, we briefly report the results of our experimentations with the more complex Arnold–Beltrami–Childress (ABC; Arnold 2014; Childress 1970) flow.

For the previously considered Roberts flow I, the modes were growing exponentially while for the ABC flow they can manifest oscillatory behavior. In addition, the ABC flow represents a more complex flow where $\mathbf{v}$ has a dependency in all 3 spatial directions. Properties such as the growth rates and the oscillation frequency of the ABC flowsi were studied numerically (Galloway & Frisch 1986; Bouya & Dormy 2012; Brandenburg & Chen 2020).

Our setup used for the ABC flow uses the same mechanism for particle flow forcing $\mathbf{v}_{\rm f}$ as the one used for the Roberts Flow I. The velocity field for the flow follows Bouya & Dormy (2012):

$$\begin{aligned} v_{{\rm f},x} &= A \sin k_0 z + C \cos k_0 y \\ v_{{\rm f},y} &= B \sin k_0 x + A \cos k_0 z \\ v_{{\rm f},z} &= C \sin k_0 y + B \cos k_0 x \end{aligned} \tag{43}$$

where $v_{{\rm f},i}$ are the components of the forcing velocity and x, y, z the particle positions. We choose $A, B, C = 1/\sqrt{3}$ such that $v_{\rm rms} = 1$, $k_0 = 2\pi/L_{\rm box} = 1$. The random ICs from Sec. 3.1 were used for the magnetic field.

The most commonly used parameters for the symmetric ABC flow are $A = B = C = 1$, resulting in a reference root-mean-square velocity of $v^{\rm ref}_{\rm rms} = \sqrt{3}$. To facilitate a clearer comparison of growth rates with the Roberts Flow I runs, we set $v_{\rm rms} = 1$ in our Swift tests. This ensures that the system size and typical velocity match those of the Roberts Flow I, with the only difference being the flow geometry.

In this setup, comparing growth rates, frequencies, and Reynolds numbers with the reference requires applying a time and coordinate transformation. Notably, Bouya & Dormy (2012) do not provide an exact definition of $R_{\rm m}$ as in Eq. 1, but instead define $R_{\rm m}$ through the induction equation:

$$\frac{\partial \mathbf{B}}{\partial t} = {\rm curl}[\mathbf{v} \times \mathbf{B}] + \frac{1}{R_{\rm m}} \Delta \mathbf{B}. \tag{44}$$

To match our convention, we performed a time translation of this equation: $t = t^{\rm ref} \cdot \sqrt{3}$. As both the reference and Swift simulations have $L = L^{\rm ref} = 2\pi$ for the flow periodicity, this leads to the velocity relation $v = v^{\rm ref}/\sqrt{3}$. Similarly, the Growth rates and frequencies relate as inverse times: $\gamma, \omega = \gamma, \omega^{\rm ref}/\sqrt{3}$. Since in both cases same the MHD equation are solved the magnetic Reynolds number relate as $R_{\rm m} = R^{\rm ref}_{\rm m} \cdot \sqrt{3}$

To measure growth rates of oscillatory modes in Swift, we track the peaks of the root-mean-square (RMS) magnetic field over the simulation volume as a function of time. In $\ln(B_{\rm rms})$ vs. t space, these peaks exhibit a linear trend. We determine the growth rate and its associated error by performing a linear fit to $\ln(B_{\rm rms})$ at the peak points.

For frequency measurements, we employ two methods: 1) Measuring the mean time interval between successive peaks.; 2) Performing a Fourier transform of the instantaneous growth rate. The first method provides high accuracy when a single dominant growing mode is present. However, it becomes less reliable when multiple oscillatory modes with similar amplitudes and growth rates coexist, as seen in mode crossing within the ABC flow. The second method's accuracy is constrained by the total simulation time. To ensure robustness, we compute the frequency using both methods and report the value with the smallest error. Note that one oscillation period in $B_{\rm rms}(t)$ corresponds to a magnetic field (MF) direction flip. Therefore, the full flip oscillation period is twice that value.

We do not measure growth rates and frequencies immediately from $t = 0$ because the modes take time to manifest in $B_{\rm rms}(t)$. Instead, we use the following time intervals: $t \in [120, 300]$ for runs far from mode transition points and $t \in [820, 1000]$ for runs near the transition. As a comparison, the reference studies extend simulations

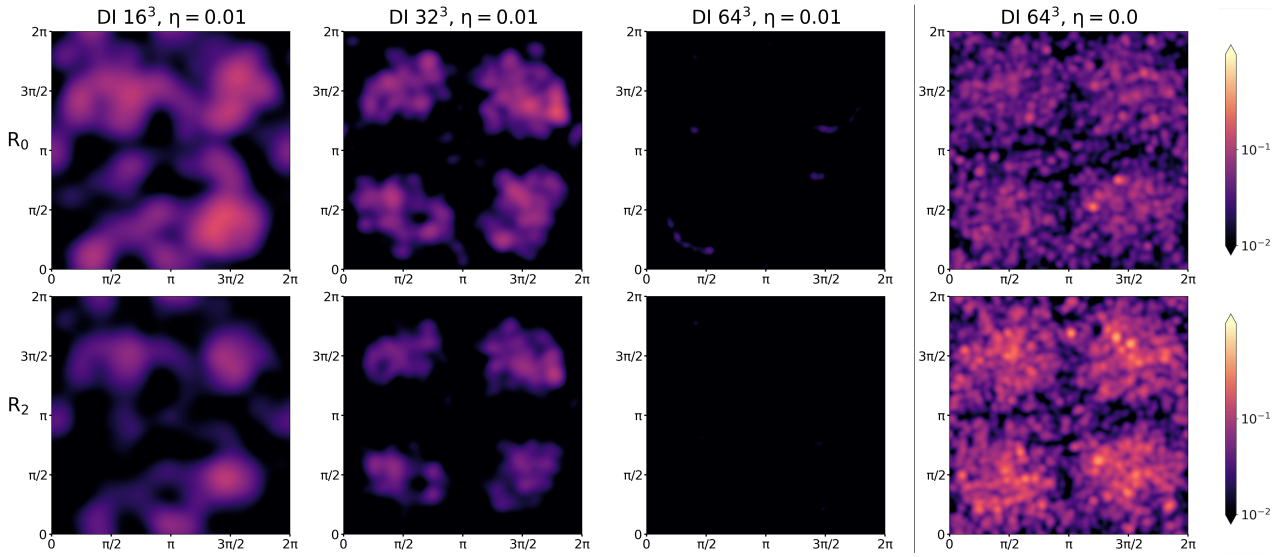

Figure 7. Density maps for dimensionless divergence error metrics $R_0 = \mathrm{div}\mathbf{B} \cdot h/|\mathbf{B}|$ (top) and $R_2 = \mathrm{div}\mathbf{B}/|\mathrm{curl}\mathbf{B}|$ (bottom) with additional cuts to reduce SPH noise. The Roberts Flow I runs were performed with $\eta = 0.01$ for 3 resolutions: 16^3 (top column), 32^3 (upper middle column), 64^3 (lower column) particles , and an additional single run with $\eta = 0$ at 64^3 resolution (right-most panel). Regions with $R_i \gtrsim 0.1$ indicate large divergence errors. The divergence errors are elevated mostly inside vortices. Resolution increase leads to decrease of divergence error metrics. Both R_0 and R_2 maps are similar in general however have some small differences at resolution scale. Divergence errors are small even in the ideal MHD limit. However, the R_2 metric shows more elevated values in this regime.

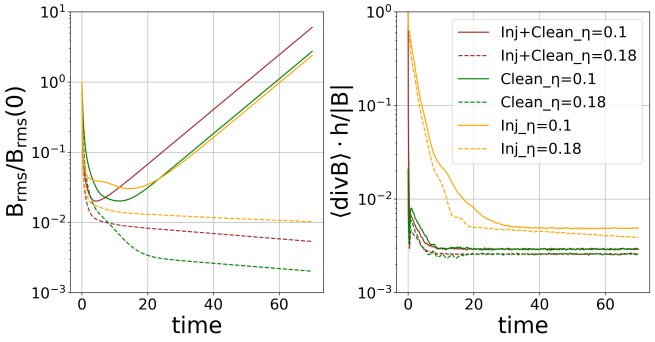

Figure 8. Evolution of the magnetic fields (left) and divergence errors (left) on a Roberts flow I test case with 32^3 particles using the direct induction (DI) MHD implementation in Swift. We perform runs with a large initial injected divergence (Inj) and the Dedner cleaning (Clean) term switched on (brown) or off (orange), and with clean ICs with the Dedner term still on (green). We perform the tests for growing (solid line) and decaying (dashed line) modes. The divergence errors decrease quickly and don't affect the magnetic field growth rates. The addition of the Dedner cleaning terms helps to decrease the error before the divergence gets cleaned by resistivity.

much more — up to $t_{\mathrm{end}}^{\mathrm{ref}} \simeq 6000$ — to achieve better mode separation. However, the selected time intervals in Swift are sufficient to accurately measure growth rates and oscillation frequencies.

We conducted simulations for magnetic Reynolds numbers in the range $R_m \in [15, 100]$. In all runs, we observe oscillatory growth of the magnetic field. The growth rate as a function of R_m is expected to have a positive region for $R_m \in [15, 30]$ and $R_m > 40$. The top plot in Figure 9 shows the growth rate versus magnetic Reynolds number for 64^3 particles in Swift, along with the rescaled results of Bouya & Dormy (2012) for $v_{\mathrm{rms}} = 1$, as described earlier. Note that in the reference, the resolution was varied with R_m, with the minimal value being 64^3). All MHD implementations in Swift follow the growth rate trends reported in the reference solutions. The critical magnetic Reynolds numbers for the onset of dynamo action are found to be $R_{\mathrm{m}}^{\mathrm{crit},1}(\mathrm{DI}) \simeq 15.6$ and $R_{\mathrm{m}}^{\mathrm{crit},1}(\mathrm{VP}) \simeq 16.7$, which are slightly larger than the reference value $R_{\mathrm{m}}^{\mathrm{crit},1} \simeq 15.5$ reported in Table 1 of Brandenburg & Chen (2020).

Similar to the Roberts Flow I results, both DI and VP implementations slightly underestimate the growth rates when compared to Bouya & Dormy (2012), with the VP method showing a somewhat larger deviation. Nonetheless, both models successfully reproduce the expected qualitative behavior, and the discrepancies remain small, with the growing modes appearing in the anticipated regimes.

The lower panel of Figure 9 illustrates the oscillation frequency of the modes as a function of R_{m}. The frequencies for both DI and VP implementations closely match the reference results outside the mode transition region. However, the transition occurs at $R_{\mathrm{m1}}^{\mathrm{Swift}} \in [40, 41.67]$, a value close to the reference transition at $R_{\mathrm{m1}}^{\mathrm{rep}} \in [41.65, 41.74]$. While the reported reference values overlap with Swift's results, a closer inspection of their growth rate knee position and frequency evolution suggests that the actual transition happens at $R_{\mathrm{m1}}^{\mathrm{plot}} \in [42.88, 43.01]$. This value differs slightly from their reported range and does not overlap with the transition values obtained for Swift.

As with Roberts Flow I, we expect a characteristic spatial distribution of the magnetic field. However, due to the oscillatory growth, these features evolve over time. To analyze this, we examined isosurfaces where $|\mathbf{B}|/B_{\mathrm{rms}} = 3$ at the time of peak $B_{\mathrm{rms}}(t)$.

According to Bouya & Dormy (2012), the isosurfaces of $\mathbf{B}$ should form diagonal "magnetic field cigars" with opposing magnetic field directions. For the 64^3 DI run, this cigar-like structure is indeed observed, as shown in Figure 10 (for $R_{\mathrm{m}} = 100$). The same structure also appears in VP runs (not shown).

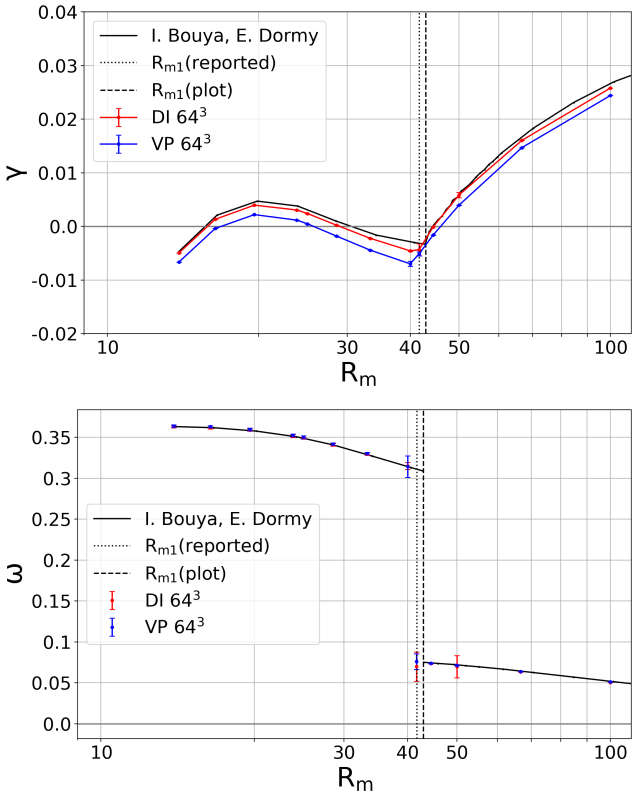

Figure 9. Growth rate (top plot) and frequency (bottom plot) vs magnetic Reynolds number for Bouya & Dormy (2012) (converted for our setup) and for Swift MHD implementations. The Swift code reproduces oscillatiry MF growth in $R_{\rm m1} \in [10, 100]$. The mode transition in Swift happens in range $R_{\rm m} \in [40, 41.67]$. The reference transition point is $R_{\rm m1}^{\rm ref} \in [41.65, 41.74]$, however, we find this value inconsistent with the transition from the plots the reference provides, $R_{\rm m1}^{\rm plot} \in [42.88, 43.01]$, from the postion of the knee in growth rate graph and the step in frequency graph (Figures 1,3 from Bouya & Dormy (2012)). Error bars in growth rate and frequency originate the calculation methods.

4 RESOLUTION AND OVERWINDING PROBLEM

Hving established that the MHD implementation in the Swift code can reproduce known results on kinematic dynamos, we now turn our attention to the link between resolution and resistivity. The discussion below follows Charbonneau (2012) with application to the finite resolution scale introduced in simulations.

4.1 Roberts Flow I minimal resistivity

The magnetic field pattern breakdown the ideal MHD limit ($\eta \to 0$, $R_{\rm m} \to \infty$) and its dependence on resolution (Figure 5) suggests a connection between the simulation resolution scale,(in our case, the smoothing length, h) and the resistivity. In the Roberts Flow I test, we have 4 vortices winding up and resistivity diffusing the magnetic field. To form a steady pattern the resistivity should thus balance the induction term in MHD equations.

To understand why the pattern breakdown appears, let us consider a simpler version of the problem, where there is one single vortex with $v_z = 0$ and a magnetic field confined to the plane. The fluid movement in the vortex of size $L_{\rm v}$ and with root mean square velocity $v_{\rm rms}$ will drag and wind the magnetic field thus increasing the magnetic field

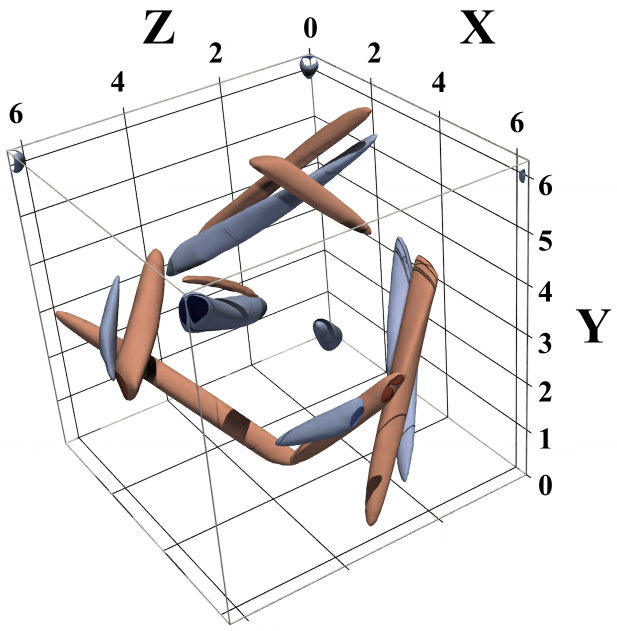

Figure 10. Isosurfaces for $|B|/B_{\rm rms} = 3$ magnetic field for the run with DI at $R_{\rm m} = 100$. Color denotes sign of $B_{\rm x}$, red is positive. Tube-like structures are visible, similar to ones observed from Figure 7 from reference Bouya & Dormy (2012), although they run at $R_{\rm m} \simeq 752$ (where we multiplied $R_{\rm m}$ by $\sqrt{3}$ to transform to $v_{\rm rms} = 1$ system). Paraview was used to visualise the 3d isosurfaces.

gradients. This process is characterised by a circulation timescale:

$$t_{\rm c} \sim \frac{L_{\rm v}}{v_{\rm rms}}. \tag{45}$$

If the magnetic field gradients have typical scale of $l_{\rm B}$ the diffusion will act on characteristic times:

$$t_{\rm d} \sim \frac{l_{\rm B}^2}{\eta}. \tag{46}$$

A steady magnetic field pattern can form if the balance occurs, *i.e.* $t_{\rm c} \sim t_{\rm d}$. This is possible when the characteristic scale of the gradient is:

$$l_{\rm B} \sim \sqrt{\frac{\eta L_{\rm v}}{v_{\rm rms}}}. \tag{47}$$

Since our SPH simulation can't resolve gradients smaller than (or of order of) the smoothing length h, the timescale balance is absent for such gradient. In this situation, the resistivity can thus, in principle, not counteract the winding, leading to the magnetic field pattern breakdown. Alternatively, this balance can also be thought as a magnetic field cascade that can or cannot be countered by cut in the spectrum from the action of the physical (Ohmic) resistivity term.

Estimates for the minimal resistivity and the maximal magnetic Reynolds number that can reached within the simulation are thus:

$$\eta_{\rm min} \sim \frac{h^2 v_{\rm rms}}{L_{\rm v}}, \qquad R_{\rm m}^{\rm max} \sim \frac{v_{\rm rms}}{\eta_{\rm min} \cdot k_{\rm f}} \sim \frac{L_{\rm v}^2}{\pi h^2}, \tag{48}$$

where $k_{\rm f} \simeq \frac{2\pi}{2L_{\rm v}}$ is flow wave vector was used. This expression relates $R_{\rm m}^{\rm max}$ to how well vortices are resolved in terms of our resolution scale h. We call the limiting resistivity the *overwinding resistivity*.

Applying this framework to the Roberts flow I case, we can compute the minimal resistivity that our method can correctly evolve.

Table 1. Overwinding resistivity for $v_{\rm rms} = 1$ and magnetic Reynolds number for the Roberts flow I test.

Resolution	h	$\eta_{\rm min}$	$R_{\rm m}^{\rm max}$
16^3	0.54	$8 \cdot 10^{-2}$	12
32^3	0.27	$2 \cdot 10^{-2}$	50
64^3	0.13	$5 \cdot 10^{-3}$	200

The Values for the runs at different resolutions are given in Table 1. We expect for the pattern to be only slightly affected when $\eta \gg \eta_{\rm min}$ and destroyed if $\eta \ll \eta_{\rm min}$. On Fig. 5, we showed the magnetic field patterns for the runs with $\eta = 0.01$. At the lowest resolution($N = 16^3$, left) the pattern is highly distorted. When the resolution is increased to $N = 32^3$ and $N = 64^3$, the pattern becomes more symmetric and develops thinner features. As expected from the analysis above, at zero resistivity (right-most panel) the balance cannot take place in principle at any resolution. The magnetic field gradients thus reach the resolution scale and the pattern disappears.

Similarly, the analysis of the growth rate as a function of resistivity (Fig. 2) confirms that for the runs at a resolution $N = 64^3$, the large deviations of the growth rate and increase in growth rate fluctuations happen around $\eta \sim 2 - 5 \cdot 10^{-3}$. This value is in good agreement with the predicted overwinding resistivity value from Table 1.

4.2 The overwinding trigger

For arbitrary types of flows present in astrophysical and cosmological applications the defining a minimal resolvable resistivity or Reynolds number is a challenging problem. We attempt to construct such a trigger here based on the considerations exposed above.

The magnetic field gradients are governed by source terms in induction equation, which can increase them:

$$\mathbf{S}_{\rm ind} = \Omega_{\rm str} + \Omega_{\rm Dedner} \tag{49}$$

Diffusion sources decrease the gradients:

$$\mathbf{S}_{\rm diff} = \Omega_{\rm Ohm} + \Omega_{\rm AR} \tag{50}$$

The gradients in the SPH simulations are bound due to the resolution scale. This rough estimate of the maximal gradient that can be resolved typically holds:

$$|\Delta \mathbf{B}| \leq \frac{2|\mathbf{B}|}{h^2}. \tag{51}$$

Therefore, there exists a limit on the diffusive source term in the induction equation, which in turn sets an upper bound on the achievable magnetic Reynolds number when magnetic field gradients reach resolution scale. If the induction source term, $\mathbf{S}_{\rm ind}$, counteracts the diffusion (*i.e.* $\mathbf{S}_{\rm diff} \cdot \mathbf{S}_{\rm ind} < 0$) and $\mathbf{S}_{\rm ind} > \mathbf{S}_{\rm ind}^{\rm max} \simeq \frac{(\eta+\eta_{AR})}{\rho} \cdot \frac{2|\mathbf{B}|}{h^2}$, then in the presence of magnetic field cascade the magnetic fields will inevitably reach resolution scales, or $|\Delta \mathbf{B}| \simeq \frac{2|\mathbf{B}|}{h^2}$. This will result in overwinding issues similar to what was found in the Roberts Flow I.

To monitor this issue we define an *overwinding trigger* as follows:

$$OW = \frac{|\mathbf{S}_{\rm ind}|}{|\mathbf{S}_{\rm diff}|} \cdot \frac{1}{2}\left(1 - \cos(\mathbf{S}_{\rm ind}, \mathbf{S}_{\rm diff})\right) \cdot \frac{h^2|\Delta \mathbf{B}|}{2|\mathbf{B}|}, \tag{52}$$

where $\mathbf{S}_{\rm diff}$ includes all diffusive sources in the simulation (physical and artificial)[3]. We expect the trigger value to be large, $OW \gtrsim 10$, if there is significant overwinding and $OW \lesssim 10^{-1}$ if the resistivity manages to counteract the winding locally and thus separate the cascade from the resolution scale.

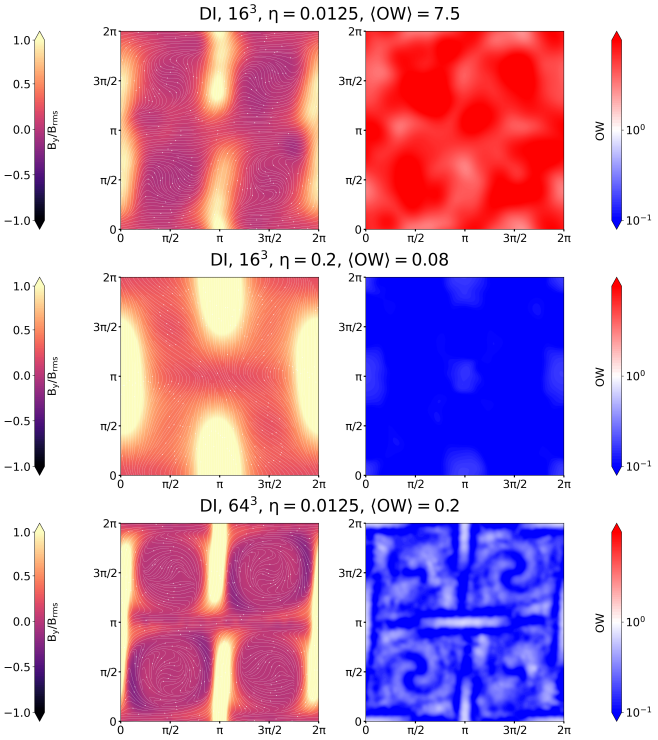

Figure 11. $B_y/B_{\rm rms}$ with magnetic field streamlines (left) and Overwinding trigger maps (right) for the Roberts flow I test in xy plane at $t = 75$, with heights adjusted to show the same feature. The top set of plots show the unresolved regime with large OW trigger values ($\langle OW \rangle \gtrsim 10$). There are two ways to enter the properly resolved regime (where $\langle OW \rangle \lesssim 10^{-1}$): with resistivity increase (middle set of plot) or with resolution increase (bottom plot). Note also that the OW metric tends to have higher values inside shear zones and inside vortices

The observed behaviour for the magnetic fields on Fig. 5 can now be reinterpreted in terms of this OW metric. When the resolution is increased, the OW trigger will decrease too since the magnetic field gradients can reach a smaller scales and thus result in a much larger $\eta \Delta \mathbf{B}$. In the highest resolution case ($N = 64^3$), this is enough to separate the magnetic field from the resolution limit. And, as expected, for the case of zero resistivity nothing prevents the magnetic fields from reaching the resolution scales resulting in the vortex pattern destruction.

We conclude this section with a visual example of the behaviour of the overwinding trigger. If trigger the values are large, $OW \gtrsim 10$, the resistivity plays only a small role in the overall evolution of the field. For this regime, OW follows the scaling:

$$OW \sim h^2 \eta^{-1}, \qquad OW|_{\rm h=const} \sim N_{\rm p}^{-2/3} \eta^{-1}, \tag{53}$$

where the second equation holds for a fixed resolution case (i.e. where there is a direct link between N and h). This scaling can be used to estimate the required resolution or resistivity needed in a simulation to prevent overwinding ($OW \lesssim 1$).

[3] Note that for this study we choose to include the Dedner cleaning term into the induction source in the trigger (eq. 52).

Such a use case is depicted in Fig. 11 for the Roberts flow test. The left panels show the B_y/B_{rms} magnetic field configuration in the xy plane at time $t = 75$ with slice heights adjusted to see the same feature whilst the right panels show the corresponding value of the OW. The top row corresponds to a setup where the field configuration cannot be properly resolved with 16^3 particles and this value of the resistivity. Either a resistivity increase from $\eta = 0.0125$ to $\eta = 0.2$ (1st to 2nd panel) or a resolution increase form 16^3 to 64^3 particles (1st to 3rd panel) are sufficient to decrease the trigger value to the regime where the vortices are fully resolved by the simulation. Of course, changing the value of the physical resistivity is not always a practical option as its value can be set by physical considerations. Increasing the resolution is then the sole option to obtained a well-behaved field with resolved kinematic dynamo growth.

The computational cost incurred then increasing resolution can be estimated as $\sim N \cdot T_{\rm sim}/\Delta t$, with $T_{\rm sim}$ the final time of the simulation and Δt the time-step size. This latter quantity is itself $\Delta t \sim \frac{h}{c_{\rm h}}$, where $c_{\rm h}$ is signal propagation speed (sound speed typically or Alfven wave speed for MHD scenarios). Assuming a constant propagation speed, the full cost is then $\sim N_{\rm p}^{\frac{4}{3}} \sim (OW \cdot \eta)^{-2}$. Thus, targeting a decrease of the OW value by an order of magnitude will cost two orders of magnitude more computational costs. On the other hand, an order of magnitude increase in the resistivity constant value will lead to the same magnitude change in OW.

Therefore, the most effective way to prevent overwinding and avoid excessive damping of relevant physical features at a given resolution is to adjust the resistivity such that $OW \simeq 1$.

5 COSMOLOGICAL MHD SIMULATIONS

Having demonstrated, that the MHD implementation in Swift code reproduced the features of the Roberts flow and ABC flow kinematic dynamo tests within the resolution-dependent Reynolds number window, we now want to demonstrate its capability to capture the basic amplification processes associated with dynamo action. In this section we explore simulations solving cosmological MHD equations, with a focus on the dynamics without considering sub-grid physics models (i.e. so-called *adiabatic* simulations).

Cosmological MHD simulations involve various flow types during structure formation, which can lead to magnetic field amplification through gravitational collapse and the stretching of magnetic field lines. Cosmological runs without resistivity can suffer from the "overwinding" problem discussed in the last section, where the magnetic field becomes excessively stretched. To mitigate this, we perform additional simulations with non-zero constant physical resistivities: first, with a typical value found in galaxy clusters, $\eta \sim 6{\times}10^{27}$ cm^2/s, and then with higher resistivity values to further minimize overwinding.

5.1 Simulation setup

Cosmological simulations with a side-length of 150 Mpc were conducted using MHD and adiabatic gas evolution, that is without including feedback or cooling physics. We perform simulations with 2×64^3 and 2×128^3 particles. This leads to a gas particles mass of $m_{\rm gas} = 8{\cdot}10^{10}{\rm M}_\odot$ and $1{\cdot}10^{10}{\rm M}_\odot$ respectively. The initial conditions for baryons and dark matter were generated using Monofonic code (Hahn et al. 2020) at a starting redshift of 63. We adopt the same cosmology as the FLAMINGO project (Schaye et al. 2023)[4]. The initial magnetic field was generated as a Beltrami field (eq. 39), with 10 waves along one axis of the box, and a root-mean-square code-comoving magnetic field strength of $\mathrm{B}_{\rm rms}^{\rm comov}(\mathrm{z}_0) = 10^{-6}\mu$G, which corresponds to $\mathrm{B}_{\rm rms}(\mathrm{z}_0) = 2.97 \cdot 10^{-2}\mu$G in physical magnetic field. This field is uncorrelated with the density structure in the ICs and does not represent a physical scenario. Note that the Beltrami field configuration was chosen to make initial conditions reproducible for runs using a vector potential scheme, which we will explore in future studies.

5.2 Ideal MHD cosmological runs

We start out analysis by an overview of the general properties of the gas distribution at $z = 0$ for our higher-resolution run.

In Fig. 12, we show the spatial distribution of an infinitely thin slice in the xy-plane, depicting the magnetic flux density (in μG, left panel), the matter over-density (middle panel), and the ratio of local velocity to the root-mean-square velocity across the simulation box (right panel). Streamlines in the magnetic flux density plot illustrate the geometry of the magnetic field in the xy-plane, while streamlines in the velocity plot represent the gas flow. The magnitude of the magnetic field strength largely follows the gas density, with denser regions exhibiting stronger magnetic fields. Gas density and velocity profiles follow the usual pattern expected from such cosmological simulations: gas forms voids and filaments, with velocity profile showing the gas flux from low density regions into dense filaments. The low-density areas display a smoother magnetic field. In the filaments, the magnetic field strength is non-uniform, both in amplitude and direction. Additionally, the velocity streamlines reveal stagnation-point-like flows, similar to those observed between vortices in the Roberts flow I. These flows, found in and along the filaments, suggest that magnetic field amplification may occur not only due to gravitational collapse but also as a result of stretching within these flows.

We now turn out attention to the value of the three error metrics we introduced in Sec. 2.4. On Fig. 13 we show the spatial distribution, in the same plane as for the previous figure, of R_0, R_1, and R_2 (eqs. 33 – 35). The SPH noise cut discussed in Sec. 2.4 has been applied using the noise estimates from equation 37. We show the error in the range $R_i \in [10^{-2}, 10^0]$.

As can be seen, a significant fraction of the simulation volume exhibits large divergence errors (R_0). However, when compared to the density and magnetic field distributions in Fig. 12, both the centers of low-density regions and the areas within filaments show lower error levels than the regions at the borders between low and high-density areas, where large density gradients are found. This indicates that the error is possibly driven by poorer quality gradient operators in such regions. The other divergence error metrics show much lower of error. The R_1 metric is below the noise cut across the entire simulation, indicating that there are no significant magnetic monopole forces acting on the particles in this setup. The R_2 metric, which estimates the monopole component of the magnetic field relative to the physical current, shows significantly fewer errors than R_0 overall, typically at a level smaller than $R_2 < 10^{-1}$. This, by design, also suggests the presence of large gradients in both the physical and monopole components of the magnetic fields at the resolution scale, with only

[4] $\Omega_{\rm CDM} = 0.2574$, $\Omega_{\rm b} = 0.0486$, $\Omega_\Lambda = 0.693922$, $h = 0.681$, $n_s = 0.967$, $A_s = 2.099 \cdot 10^{-9}$,

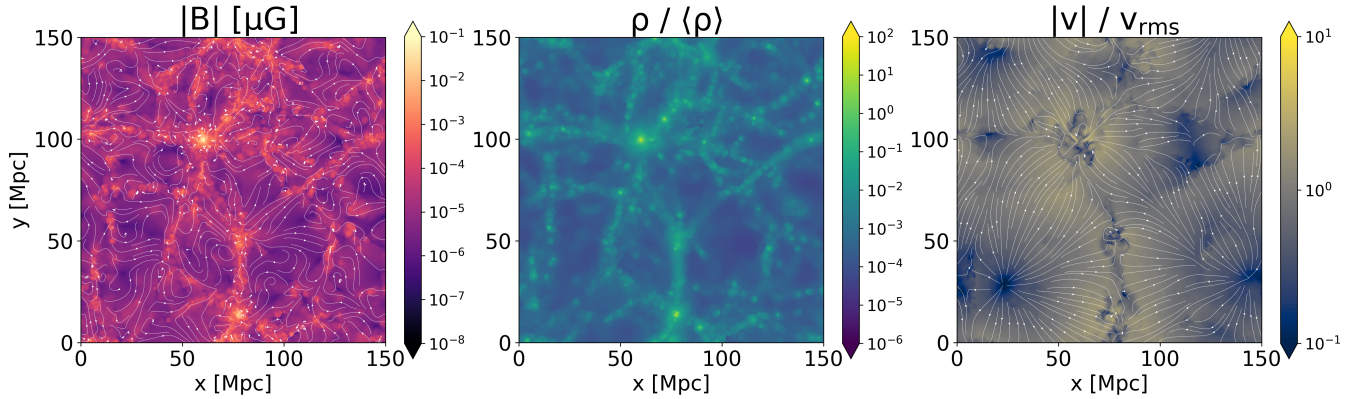

Figure 12. Magnetic field in micro-Gauss with field streamlines (left), gas over-density (center) and ratio of velocity to root-mean-square velocity of the gas with flow streamlines (right) for adiabatic cosmological run with zero resistivity at redshift $z = 0$ with 128^3 particles using the direct induction SPMHD implementation in the Swift code. The density map shows, as expected, the formation of voids and filaments, while the velocity profile shows the flow of gas from voids into filaments and high density nodes. The magnetic field amplitude distribution mostly follows the density.

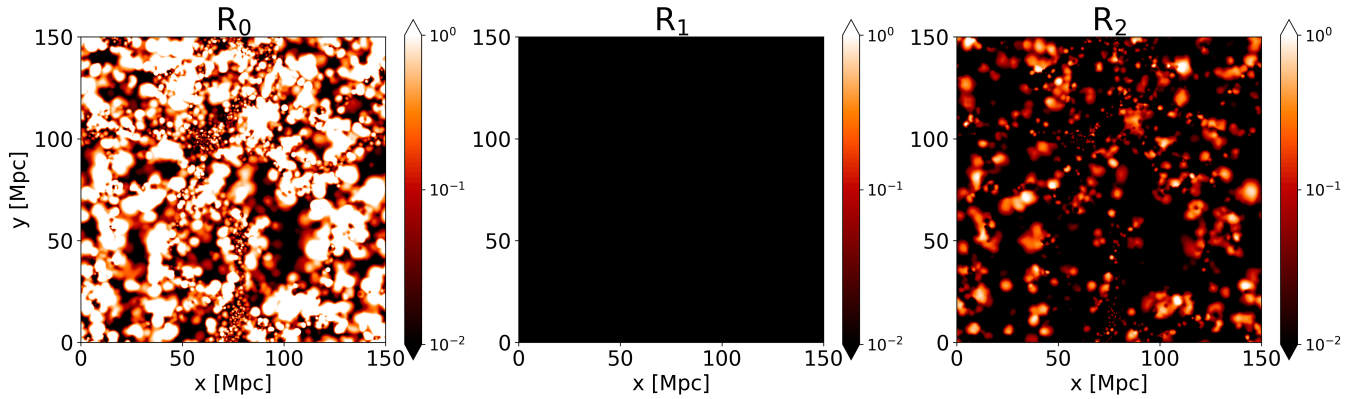

Figure 13. Divergence error metrics (eqs. 33 – 35) for our adiabatic cosmological run with zero resistivity at redshift $z = 0$ and 128^3 particles using the direct induction SPMHD implementation in Swift. The R_0 metric indicates that there are regions with large divergence errors, however, the R_2 error metric lights up less showing that at some places with large R_0 the physical field is more significant and thus the divergence error may not influence the dynamics of the field. Therefore, there are large magnetic field gradients at resolution scale. Since the R_1 is below our noise cut everywhere, we expect no unphysical (monopole) force acting on the matter evolution. The R_0 errors have large volume filling fraction and concentrate at density gradients.

some regions (indicated by R_2) exhibiting a significant monopole component.

5.3 Non-ideal MHD cosmological runs

We now consider the case of cosmological simulations with Ohmic resistivity. We run the same setup as explored above but start at 8× lower mass resolution and using a a constant physical resistivity $\eta = 6 \times 10^{27}$ cm^{2}s^{-1}; a value typical for galaxy clusters (Bonafede et al. 2011). For such a simulation, we found that the the OW (eq. 52) is very high everywhere. Its mean value was found to be $\langle OW \rangle \sim 10^4$, indicating that magnetic field gradients are under-resolved.

Since we expect the overwinding metric to follow the scaling from eq. 53, two approaches can mitigate this issue and achieve a better resolved kinematic dynamo for the fields (i.e. $\langle OW \rangle \lesssim 1$): (1) increasing the resistivity to $\eta \gtrsim 6 \times 10^{31}$ cm^{2}s^{-1} or (2) increasing the number of particles.

However, it is worth noting that, in a typical cosmological setup, increasing the number of particles may introduce new substructures, which could again be under-resolved, but on smaller scales. In regions where a mostly uniform density is expected, such as voids, reducing the trigger values from 10^4 requires increasing the particle count sufficiently to decrease h/L_B by at least a factor of 100, a challenging demand.

We showed the effect of changing resolution or the value of resistivity on the Roberts flow I test in Sec. 4.2. We now perform the same type of experiments in our cosmological setup, in order to demonstrate the importance of monitoring OW also in SPMHD applications beyond tests.

To this end, we conducted three more simulations at the same resolution (64^3 particles) but with three different resistivity values: $\eta = 3\times10^{30}$ cm^{2}s^{-1}, $\eta = 3\times10^{31}$ cm^{2}s^{-1}, and $\eta = 9\times10^{31}$ cm^{2}s^{-1}, corresponding to, respectively, the first, second, and last rows of Fig. 14. The figure presents the spatial distribution of an infinitely thin slice in the xy-plane at redshift zero, showing the magnetic flux density (in μG, left), the divergence error R_0 (including our noise cut, middle column), and the overwinding trigger values (right column). Streamlines in the magnetic flux density plot illustrate the field geometry. From top to bottom, both resolution and resistivity vary across the panels, as indicated on the right of the figure.

At the lowest resistivity, $\eta \simeq 3\times10^{30}$ cm^2/s (top row), the R_0 profile reveals significant volume-filling errors, while the overwinding trigger remains high at $\langle OW \rangle \simeq 6.95$.

With a tenfold increase in resistivity (second row of Fig. 14), the

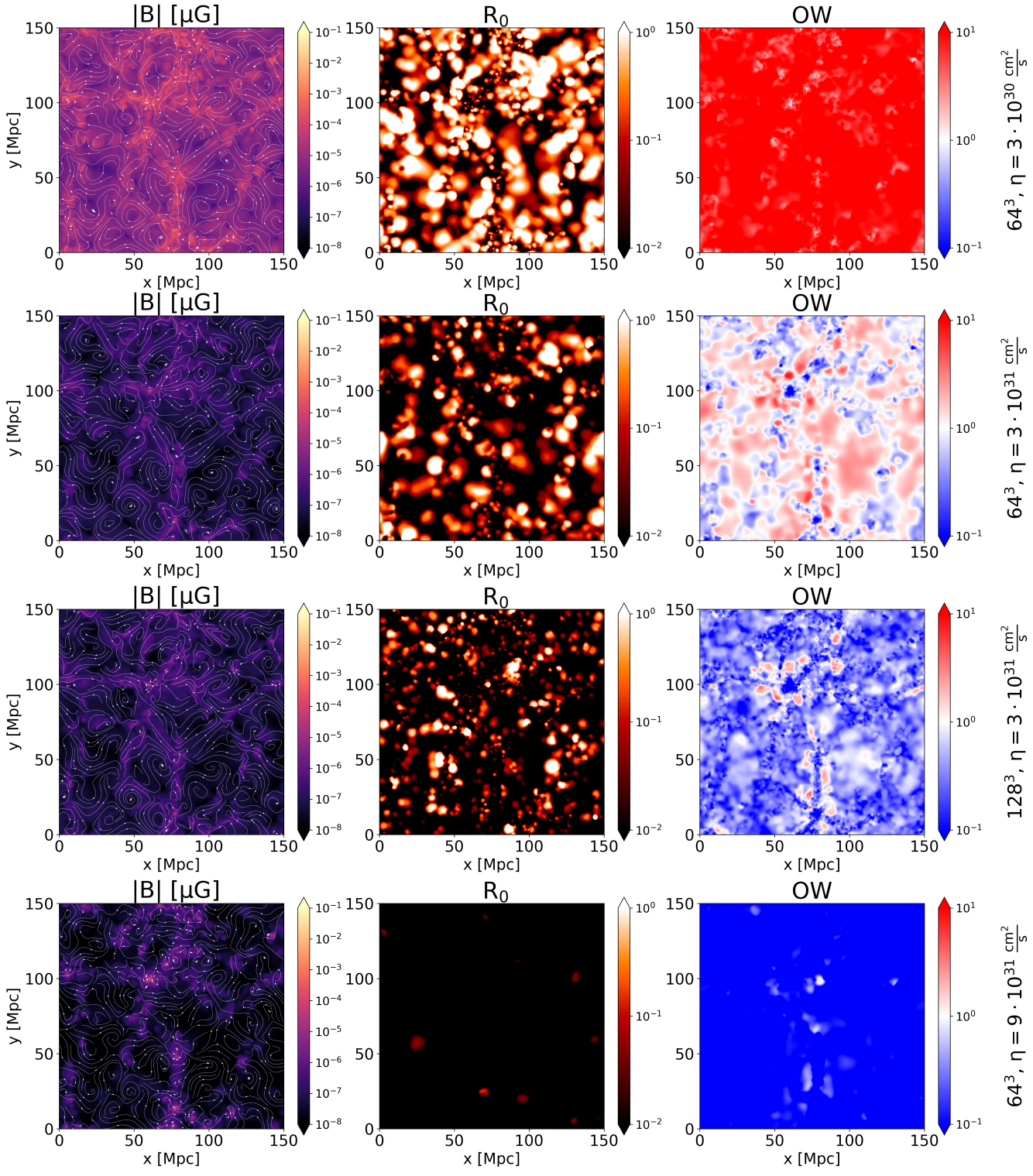

Figure 14. Maps of the magnetic field B (in μG), error metric R_0, and OW trigger values in our adiabatic cosmological simulations at $z = 0$ run with the direct induction SPMHD implementation in Swift for a 64^3 particles run with $\eta = 3 \cdot 10^{30}$ cm^{2}s^{-1} (top row), $\eta = 3 \cdot 10^{31}$ cm^{2}s^{-1} (second row), a run with the same resistivity but with 128^3 particles (third row), and a run with 64^3 particles but $\eta = 9 \cdot 10^{31}$ cm^{2}s^{-1} (bottom row). Increasing the resistivity (1st to 2ns row) leads to a decrease in the OW trigger values and a reduction in the volume-filling fraction of divergence errors, while also significantly decreasing the magnetic field magnitude. Increasing the resolution from the second to the third row further reduces the OW trigger, though the overall R_0 filling fraction remains similar. From the second to the bottom row, a further increase in resistivity significantly reduces the OW trigger while bringing divergence error levels to an acceptable range ($R_0 < 10^{-1}$). At the same time, the magnetic field structure changes slightly: some filament regions experience damping, while high-density regions exhibit increased magnetic field strength.

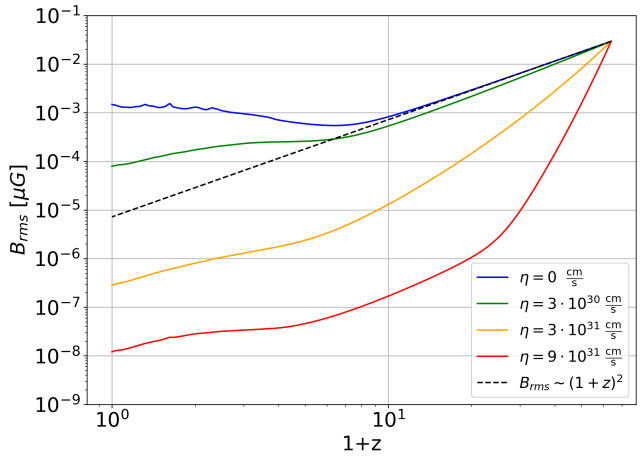

Figure 15. Root mean square magnetic field vs scale-factors for the adiabatic cosmological runs with 64^3 particles with $\eta = 0; 3 \cdot 10^{30}; 3 \cdot 10^{31}; 9 \cdot 10^{31}; 10^{33} \mathrm{cm}^2\mathrm{s}^{-1}$ (corresponding to the $z = 0$ slices shown in Fig. 13 and 14). A large constant physical resistivity strongly dampens the initial magnetic field amplitude. The evolution is consistent with cosmological expansion around $z \simeq 10$, followed by amplification near $z \simeq 0$.

overwinding trigger decreases to $\langle OW \rangle \simeq 0.56$, which is close to the expected value of 0.69 from the OW resistivity scaling (eq. 53). The OW trigger maps are non-uniform, showing higher values in low-density regions compared to high-density regions. The volume-filling fraction of R_0 errors is also reduced, though some regions still exhibit $R_0 > 1$. Additionally, a significant decrease in magnetic field magnitude is observed, while its overall morphology remains largely preserved.

With a further three-fold increase in resistivity (bottom row of Fig. 14), the overwinding trigger $\langle OW \rangle$ deviates from the expected scaling, decreasing more rapidly to $\langle OW \rangle \simeq 0.01$. However, regions with $OW \simeq 1$ persist near the filament edges. The global error levels are significantly reduced, remaining within an acceptable range of $R_0 < 10^{-1}$ throughout. Comparing the second and bottom rows of Fig. 14, the magnetic field amplitude shows different trends: it is dampened in some regions along the filaments, while inside the filaments and at the nodes, it becomes amplified.

Finally, we increased the resolution of the simulation with $\eta = 3\ \mathrm{cm}^2\mathrm{s}^{-1}$ from 64^3 to 128^3 particles in order to locally reduce the smoothing length and mitigate overwinding. The results from this higher-resolution simulation are shown on the third row of Fig. 14. The resolution change led to a global reduction of the overwinding trigger in both high- and low-density regions, as expected from the scaling of the metric. However, some areas near the filament edges still exhibit large overwinding. Meanwhile, the volume-filling fraction of R_0 remains largely unchanged with only a small reduction. Recall though that we found to the large divergence error to not be dynamically relevant in our analysis of the ideal-MHD case.

5.4 Discussion

As we just demonstrated, our Swift-based SPMHD adiabatic cosmological simulations (i.e. without additional sub-grid physics) produce reasonable magnetic field, density distributions, and velocity slices, thus demonstrating the general reliability of the implemented MHD model. However, the accuracy of the results is affected by large errors, which are primarily attributed to unresolved gradients in both the physical and monopole components of the magnetic field. These errors tend to concentrate around density gradients, suggesting a need for additional numerical techniques to mitigate their impact.

While the addition of constant physical resistivity helps reduce both R_0 and OW, it also significantly dampens the magnetic fields. This is, thus, an undesirable solution in many cases.

To illustrate this, we show on Fig. 15 the evolution of the root-mean-square magnetic field strength, B_{rms} (in μG), as a function of redshift for our simulations with 64^3 particles with zero physical resistivity (blue lines), as well as for the simulations corresponding to the first (green), second (yellow), and last (red) rows of Fig. 14. The dashed line indicates the cosmological dilution of the initial magnetic field if no MHD forces were present.

The expected solution is that of cosmological expansion line (black dashed) for $z > 10$, followed by amplification from structure formation.

A significant magnetic field damping is observed at high redshifts ($z > 10$) for non-zero resistivity. This occurs because, at earlier times, when the Universe is smaller and magnetic field gradients are on smaller scales, the constant resistivity term has a stronger effect. As a result, a substantial initial damping occurs.

Nevertheless, after the initial damping at $z \lesssim 10$, all runs with resistivity exhibit a similar evolution. Initially, they follow the same tilt as the evolution driven by cosmological expansion, followed then by amplification near z = 0.

A potential solution is to implement an adaptive artificial resistivity that dynamically responds to the overwinding metric, maintaining it around $OW \simeq 1$. In the case for runs above this approach could reduce excessive damping at high redshifts while still effectively controlling overwinding at z = 0. However, any such implementation should be designed to not violate astrophyiscs considerations. Future work should explore this adaptive method to balance error correction with physical accuracy in evolving magnetic fields.

6 CONCLUSIONS

In this paper, we presented the results of new Swift SPH MHD implementations using direct induction (DI) and vector potential (VP) methods for kinematic dynamo tests. Both implementations successfully reproduce the expected qualitative and quantitative features when compared to other codes.

For Roberts Flow I, growth rates (Figure 2) and the spatial distribution of the magnetic field (Figure 1) closely match Pencil code results, demonstrating numerical convergence (Figure 4). Additionally, we examined ABC flow, where magnetic field structures (Figure 10), growth rates, and oscillation frequencies (Figure 9) were also well reproduced compared to reference results.

Regarding divergence errors, VP maintains error levels below 20% across all resistivities. For DI, however, divergence errors increase at low resistivity unless Dedner cleaning is applied (Figure 6). With cleaning, the errors remain within an acceptable range. Additionally, we assessed the stability of DI with divergence cleaning by introducing a significant initial monopole component in the magnetic field in the Roberts Flow I setup. In this scenario, Dedner cleaning effectively removed the errors, which did not significantly impact growth rates (Figure 8).

To better track spatial divergence errors, we introduced additional monitoring quantities, which, in the low-resistivity regime, revealed regions not captured by conventional diagnostics (Figure 7). We also established and tested the overwinding metric - a criterion for the

onset of a numerically unresolved dynamo regime in Roberts Flow I (Eq. 52).

Furthermore, we performed several adiabatic cosmological runs (without subgrid modeling) with zero resistivity. These runs produced reasonable magnetic field, density, and velocity distributions (Figure 12) but exhibited large divergence errors, particularly near density gradients (Figure 13). By introducing a constant resistivity term based on the overwinding metric, we significantly reduced divergence errors while largely preserving the magnetic field structure (Figure 14). However, a notable drawback of using constant resistivity is the initial overdamping of the magnetic field magnitude (Figure 15). This issue could potentially be mitigated by an adaptive resistivity approach, which future work should explore to balance error correction with the preservation of physical dynamics.

In conclusion, both the DI and VP SPMHD implementations in Swift successfully reproduce the action of kinematic dynamo in controlled environments such as in the Roberts flow I and ABC flows. We demonstrated that poor numerical behaviour at high Reynolds numbers can be identified using the overwinding trigger and divergence error metrics. Additionally, the code qualitatively reproduces cosmological simulations, solving the MHD equations in an expanding universe without subgrid physics. Introducing a constant resistivity term based on the overwinding metric effectively reduced divergence errors over the course of the cosmological simulation. To further improve the implementations, an adaptive artificial resistivity scheme, dynamically adjusted based on local overwinding, could be implemented. This approach would better control divergence errors and enhance the field's smoothness while minimizing the risk of excessive magnetic field damping.

DATA AVAILABILITY

The SWIFT simulation code is entirely public, including the examples presented in this work. It can be found alongside an extensive documentation on the website of the project: `www.swiftsim.com`. The Pencil Code (Pencil Code Collaboration et al. 2021), is freely available on `https://github.com/pencil-code`. The simulation setups and corresponding input and reduced output data for the Pencil Code runs are freely available on `http://norlx65.nordita.org/~brandenb/projects/Roberts-Flow-Test`.

REFERENCES

Archontis V., Dorch S. B. F., Nordlund A., 2002, A&A, 397, 393–399
Arnold V. I., 2014, Sur la topologie des écoulements stationnaires des fluides parfaits. Springer Berlin Heidelberg, Berlin, Heidelberg, pp 15–18, doi:10.1007/978-3-642-31031-7_3, https://doi.org/10.1007/978-3-642-31031-7_3
Arámburo-García A., Bondarenko K., Boyarsky A., Nelson D., Pillepich A., Sokolenko A., 2021, MNRAS, 505, 5038–5057
Arámburo-García A., Bondarenko K., Boyarsky A., Neronov A., Scaife A., Sokolenko A., 2022, MNRAS, 515, 5673–5681
Attia M., Teyssier R., Katz H., Kimm T., Martin-Alvarez S., Ocvirk P., Rosdahl J., 2021, MNRAS, 504, 2346–2359
Baggaley A., Shukurov A., Barenghi C., Subramanian K., 2009, AN, 331, 46–62
Biermann L., Schlüter A., 1951, Phys. Rev., 82, 863
Bonafede A., Dolag K., Stasyszyn F., Murante G., Borgani S., 2011, MNRAS, 418, 2234–2250
Bondarenko K., Boyarsky A., Korochkin A., Neronov A., Semikoz D., Sokolenko A., 2022, A&A, 660, A80
Borrow J., Schaller M., Bower R. G., Schaye J., 2021, MNRAS, 511, 2367–2389
Bouya I., Dormy E., 2012, Physics of Fluids, 25, 037103
Brandenburg A., 2003, in Ferriz-Mas A., Núñez M., eds, , Advances in Nonlinear Dynamics. CRC Press, p. 269, doi:10.1201/9780203493137.ch9
Brandenburg A., 2010, MNRAS, 401, 347
Brandenburg A., Chen L., 2020, Journal of Plasma Physics, 86
Brandenburg A., Dobler W., 2002, Computer Physics Communications, 147, 471
Brandenburg A., Ntormousi E., 2023, ARA&A, 61, 561
Brandenburg A., Subramanian K., 2005, Physics Reports, 417, 1–209
Bryan G. L., et al., 2014, ApJS, 211, 19
Børve S., Omang M., Trulsen J., 2001, ApJ, 561, 82
Charbonneau P., 2012, Solar and stellar dynamos, 2013 edn. Saas-Fee Advanced Course, Springer, Berlin, Germany
Childress S., 1970, Journal of Mathematical Physics, 11, 3063
Clarke A. T., Davies C. J., Ruprecht D., Tobias S. M., 2020, Journal of Computational Physics: X, 7, 100057
Dedner A., Kemm F., Kröner D., Munz C.-D., Schnitzer T., Wesenberg M., 2002, Journal of Computational Physics, 175, 645
Devlen E., Brandenburg A., Mitra D., 2013, MNRAS, 432, 1651–1657
Dolag K., Stasyszyn F., 2009, MNRAS, 398, 1678–1697
Durrer R., Neronov A., 2013, A&ARv, 21
Galloway D., Frisch U., 1986, GApFD, 36, 53
Hahn O., Rampf C., Uhlemann C., 2020, MNRAS, 503, 426–445
Han J., 2017, ARA&A, 55, 111
Hopkins P. F., Raives M. J., 2015, MNRAS, 455, 51–88
Jackson J. D., 1999, Classical electrodynamics, 3rd ed. edn. Wiley, New York, NY, http://cdsweb.cern.ch/record/490457
Karapiperis O., et al., 2025, in prep.
Kaviraj S., et al., 2017, MNRAS, 467, 4739
Korochkin A., Kalashev O., Neronov A., Semikoz D., 2021, ApJ, 906, 116
Langer M., Durrive J.-B., 2018, Galaxies, 6
Liu Y., Kretschmer M., Teyssier R., 2022, MNRAS
Marinacci F., Vogelsberger M., Mocz P., Pakmor R., 2015, MNRAS, 453, 4000–4020
Mikhailov E. A., Andreasyan R. R., 2021, Open Astronomy, 30, 127
Mtchedlidze S., Domínguez-Fernández P., Du X., Brandenburg A., Kahniashvili T., O'Sullivan S., Schmidt W., Brüggen M., 2022, ApJ, 929, 127
Nelson D., et al., 2019, Computational Astrophysics and Cosmology, 6, 2
Neronov A., Vovk I., 2010, Science, 328, 73–75
Pakmor R., Springel V., 2013, MNRAS, 432, 176–193
Pakmor R., Bauer A., Springel V., 2011, MNRAS, 418, 1392–1401
Pencil Code Collaboration et al., 2021, JOSS, 6, 2807
Pfrommer C., Werhahn M., Pakmor R., Girichidis P., Simpson C. M., 2022, MNRAS, 515, 4229–4264
Powell K. G., Roe P. L., Linde T. J., Gombosi T. I., De Zeeuw D. L., 1999, Journal of Computational Physics, 154, 284
Price D. J., 2012, Journal of Computational Physics, 231, 759–794
Price D. J., Monaghan J. J., 2005, MNRAS, 364, 384
Price D. J., et al., 2018, Publ. Astron. Soc. Australia, 35
Rheinhardt M., Devlen E., Rädler K.-H., Brandenburg A., 2014, MNRAS, 441, 116–126
Rieder M., Teyssier R., 2016, MNRAS, 457, 1722–1738
Roberts G. O., 1972, Philosophical Transactions of the Royal Society of London. Series A, Mathematical and Physical Sciences, 271, 411
Rogachevskii I., 2021, Turbulent Transport of Magnetic Fields. Cambridge University Press, p. 89–154
Ruzmaikin A., Sokoloff D., Shukurov A., 1988, Nature, 336, 341
Schaller M., et al., 2024, MNRAS, 530, 2378–2419
Schaye J., et al., 2023, MNRAS, 526, 4978–5020
Schekochihin A. A., Haugen N. E. L., Brandenburg A., Cowley S. C., Maron J. L., McWilliams J. C., 2005, ApJ, 625, L115–L118
Schober J., Schleicher D., Federrath C., Glover S., Klessen R. S., Banerjee R., 2012, ApJ, 754, 99

Stasyszyn F. A., Elstner D., 2015, Journal of Computational Physics, 282, 148
Stasyszyn F. A., Dolag K., Beck A. M., 2012, MNRAS, 428, 13–27
Teyssier R., Fromang S., Dormy E., 2006, Journal of Computational Physics, 218, 44–67
Tilgner A., Brandenburg A., 2008, MNRAS, 391, 1477–1481
Tjemsland J., Meyer M., Vazza F., 2024, ApJ, 963, 135
Tricco T. S., Price D. J., Bate M. R., 2016, Journal of Computational Physics, 322, 326
Vazza F., Brüggen M., Gheller C., Wang P., 2014, MNRAS, 445, 3706–3722
Vazza F., Paoletti D., Banfi S., Finelli F., Gheller C., O'Sullivan S. P., Brüggen M., 2020, MNRAS, 500, 5350
Violeau D., 2015, Fluid Mechanics and the SPH Method: Theory and Applications. Oxford University Press, https://books.google.nl/books?id=JG41rgEACAAJ
Vogelsberger M., Marinacci F., Torrey P., Puchwein E., 2020, Nature Reviews Physics, 2, 42
Wang P., Abel T., 2009, ApJ, 696, 96
Widrow L. M., 2002, Rev. Mod. Phys., 74, 775
Williamson J. H., 1980, Journal of Computational Physics, 35, 48
Wissing R., Shen S., 2020, A&A, 638, A140

This paper has been typeset from a TEX/LATEX file prepared by the author.